

# A 3D Non-Stationary MIMO Channel Model for Reconfigurable Intelligent Surface Auxiliary UAV-to-Ground mmWave Communications

Baiping Xiong<sup>ID</sup>, Zaichen Zhang<sup>ID</sup>, *Senior Member, IEEE*, Hao Jiang<sup>ID</sup>, *Member, IEEE*, Jiangfan Zhang<sup>ID</sup>, *Member, IEEE*, Liang Wu<sup>ID</sup>, *Senior Member, IEEE*, and Jian Dang<sup>ID</sup>, *Senior Member, IEEE*

**Abstract**—Unmanned aerial vehicle (UAV) communications exploiting millimeter wave (mmWave) can satisfy the increasing data rate demands for future wireless networks owing to the line-of-sight (LoS) dominated transmission and flexibility. In reality, the LoS link can be easily and severely blocked due to poor propagation environments such as tall buildings or trees. To this end, we introduce a reconfigurable intelligent surface (RIS), which passively reflects signals with programmable reflection coefficients, between the transceivers to enhance the communication quality. Specifically, in this paper we generalize a three-dimensional (3D) non-stationary wideband end-to-end channel model for RIS auxiliary UAV-to-ground mmWave multiple-input multiple-output (MIMO) communication systems. By modeling the RIS as a virtual cluster, we study the *power delivering capability* of RIS as well as the *fading characteristic* of the proposed channel model. Important channel statistical properties are derived and thoroughly investigated, and the impact of RIS reflection phase configurations on these statistical properties is studied, which provides guidelines for the practical system design. The agreement between theoretical and simulated as well as measurement results validate the effectiveness of the proposed channel model.

**Index Terms**—Reconfigurable intelligent surface, non-stationary UAV-to-ground mmWave channel model, power delivering capability, reflection phase, statistical properties.

Manuscript received June 26, 2021; revised October 26, 2021; accepted January 6, 2022. Date of publication January 20, 2022; date of current version July 12, 2022. This work was supported in part by the NSFC under Project 6196206005, Project 62101275, Project 62171127, and Project 61971136; in part by the Jiangsu NSF Project under Grant BK20200820; and in part by the Research Fund of National Mobile Communications Research Laboratory. The associate editor coordinating the review of this article and approving it for publication was R. He. (*Corresponding authors: Zaichen Zhang; Hao Jiang.*)

Baiping Xiong is with the National Mobile Communications Research Laboratory, Frontiers Science Center for Mobile Information Communication and Security, Southeast University, Nanjing 210096, China (e-mail: xiongbp@seu.edu.cn).

Zaichen Zhang, Liang Wu, and Jian Dang are with the National Mobile Communications Research Laboratory, Frontiers Science Center for Mobile Information Communication and Security, Southeast University, Nanjing 210096, China, and also with Purple Mountain Laboratories, Nanjing 211111, China (e-mail: zczhang@seu.edu.cn; wuliang@seu.edu.cn; dangjian@seu.edu.cn).

Hao Jiang is with the College of Artificial Intelligence, Nanjing University of Information Science and Technology, Nanjing 210044, China, and also with the National Mobile Communications Research Laboratory, Frontiers Science Center for Mobile Information Communication and Security, Southeast University, Nanjing 210096, China (e-mail: jianghao@nuist.edu.cn).

Jiangfan Zhang is with the Department of Electrical and Computer Engineering, Missouri University of Science and Technology, Rolla, MO 65409 USA (e-mail: jiangfanzhang@mst.edu).

Color versions of one or more figures in this article are available at <https://doi.org/10.1109/TWC.2022.3142437>.

Digital Object Identifier 10.1109/TWC.2022.3142437

## I. INTRODUCTION

RECENTLY, the research on next generation wireless networks has attracted many attentions from both academia and industry, among which the space-air-ground integrated network (SAGIN) has been considered promising to realize global coverage [1]. As an integral part of the SAGIN, unmanned aerial vehicle (UAV) communications have been in rapid development for both civil and military applications due to its low cost and flexibility [2]. Meanwhile, the advantages of applying millimeter wave (mmWave) in terrestrial communications have also motivated the usage of mmWave in UAV communications to satisfy the increasing bandwidth and data rate demands [3]. UAV communications exploiting mmWave will significantly boost the system throughput because of the line-of-sight (LoS) dominated transmission, whose performance can be easily and severely deteriorated when the LoS link gets blocked. Thanks to the development of meta-surface, reconfigurable intelligent surface (RIS), which has the ability to manipulate the impinging waves towards the destinations constructively, has been considered promising to address this issue in a low-cost and energy efficient manner [4], whose design and performance evaluation require an accurate and in-depth understanding of the channel propagation characteristics.

### A. Prior Work

Owing to the potential of RIS, there have been many efforts in the research on RIS-assisted wireless communications, which generally lies in two aspects, one is the optimization of RIS reflection phase to achieve higher data rate or enhanced coverage and the other is the use of RIS to boost the development of new technologies. For the first aspect, specifically in the general area of RIS-assisted UAV or mmWave communications, the authors in [5] jointly designed the UAV's trajectory and passive beamforming of RIS to maximize the average achievable rate of a RIS-assisted UAV communication system for obtaining substantially communication quality improvement. The authors in [6] achieved panoramic signal reflection of RIS by deploying the RIS in an aerial platform; in which they adopted a uniform linear array (ULA) configured RIS, which is hard to implement for the RIS with a large number of units. Moreover, in [7] the authors studied the hybrid precoding design of a RIS aided multi-user mmWave communication system, where the results show desirable performance gain

in symbol error rate with the assistance of RIS. The channel capacity of a RIS-assisted indoor mmWave communication system is optimized in [8], in which the system model was designed for two-dimensional (2D) propagation scenarios and only considered the propagation through RIS. For the second aspect of applying RIS to boost the development of new technologies, the authors in [9] considered the use of RISs in wireless communication transceivers design for achieving cost effective communications. RIS aided non-orthogonal multiple access (NOMA) network for energy efficient communications was studied in [10]. RIS-based index modulation for achieving spectral efficient communications in the context of beyond multiple-input multiple-output (MIMO) solutions was proposed in [11]. Moreover, the potential of RIS in joint localization and communications was investigated in [12].

The development of RIS-assisted communications requires an in-depth understanding of the underlying channel characteristics. Thus far, there have been several research results on the path loss modeling of RIS systems [13]- [16], whereas the studies on multipath small-scale statistical channel modeling are still in infancy, let alone the channel modeling for RIS auxiliary UAV mmWave communications. By partitioning the large RIS into tiles, [17] developed a statistical channel model, which ignored the practical orientation angle of RIS. The authors in [18] presented a three-dimensional (3D) non-stationary channel model for RIS-assisted MIMO systems, but the model was dedicated for sub-6 GHz terrestrial communications scenarios. In [19], the authors developed a statistical channel model for RIS-assisted mmWave communications, which was restricted for narrowband stationary systems. These channel models, in reality, cannot be adapted for RIS auxiliary UAV mmWave communications due to the unique propagation characteristics. In general, the UAV flies in 3D space, causing the non-stationarity of the channel. The mmWave channels are typical sparsely-scattered with small angle spread, leading to the sparsity of the channel [20]. Moreover, the RIS reflects the signals by introducing programmable coefficients without processing, which is significantly different from the relays. These all should be carefully considered in RIS auxiliary UAV-to-ground mmWave channel modeling.

### B. Motivations

The channel models in aforementioned studies, which are mainly based on simplistic mathematical models with the channel coefficients generated by complex Gaussian random variables, will suffer from a lack of accuracy and generality to describe the realistic RIS auxiliary UAV communication environments. The RIS, which has no sensing capability, generally reflects the waves without further processing, and only the end-to-end propagation statistics between the transceiver are of interest in system design and algorithm validations. Furthermore, UAV communications at mmWave bands have shown its potential in sustaining bandwidth and data rate demands for high throughput applications, but the corresponding channel properties when incorporating with RIS still remains unknown. These motivate us to study the underlying channel characteristics in RIS auxiliary UAV-to-ground mmWave communications and develop statistical channel models for

characterizing the end-to-end statistics of the realistic RIS auxiliary UAV-to-ground mmWave communication channels.

### C. Main Contributions

In this paper, we develop a 3D non-stationary wideband MIMO channel model for RIS auxiliary UAV-to-ground mmWave communications when the direct propagation path between the UAV and ground receiver gets blocked. The major contributions and novelties of this paper are summarized as follows:

- We develop a 3D non-stationary wideband MIMO UAV channel model at mmWave bands for multipath small-scale fading of the propagation channel between the UAV and ground MR with the assistance of RIS, which has the ability to capture the non-stationary properties of UAV channels and sparsity of mmWave channels. By appropriately adjusting the model parameters, it can be adapted for various RIS-assisted communication scenarios.
- Different from the existing channel models for RIS-assisted communications, the proposed channel model considers an *end-to-end propagation model* from the UAV to MR by modeling the RIS as *virtual cluster* and RIS units as *virtual scatterers*. In this case, different RIS units share similar distances and angles. Although we model the RIS by virtual cluster, it is different from the conventional clusters in [21] and [22] owing to the programmability of RIS reflection coefficients. Then, we show that the proposed channel model is characterized by Rician fading under optimal and discrete reflection phase configurations, whereas by Rayleigh fading under random uniform reflection phase configuration.
- The *power delivering capability* of RIS is investigated, which embodies guidelines for the practical design and deployment of RIS for higher power gains. Perfect agreement between theoretical and simulated as well as measurement results validate the proposed model. The results highlight the advantage of *discrete configuration* of the RIS reflection phases.

The remainder of this paper is organized as follows. Section II presents the system channel model, where a 3D non-stationary UAV-to-ground mmWave channel model with the assistance of RIS is proposed. In Section III, the important statistical properties of the proposed channel model are derived and analyzed. The results and discussions are presented in Section IV. Finally, we draw conclusions in Section V.

*Notation:* Throughout this paper, non-boldface, boldface lowercase, and boldface uppercase letters denote scalar, vector, and matrix, respectively;  $|\cdot|$ ,  $\|\cdot\|$ ,  $(\cdot)^T$ , and  $(\cdot)^*$  stand for absolute value,  $\ell_2$  norm, transpose, and complex conjugate, respectively;  $\mathbb{E}(\cdot)$ ,  $Var(\cdot)$ ,  $Re(\cdot)$ ,  $Im(\cdot)$ , and  $Cov(\cdot)$  take the expectation, variance, real part, imaginary part, and covariance, respectively.

## II. SYSTEM CHANNEL MODEL

As shown in Fig. 1, let us consider a UAV MIMO communication scenario at mmWave bands, where the direct propagation path between the UAV and ground MR is severely blocked due to the poor propagation environments, like buildings or

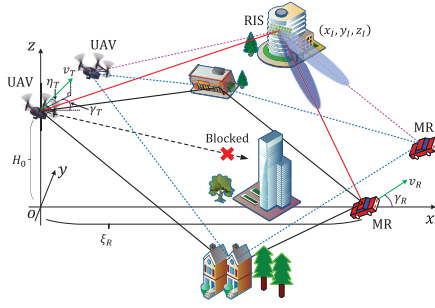


Fig. 1. A physical illustration of the proposed 3D channel model for RIS auxiliary UAV-to-ground mmWave communications. The direct path between UAV and MR is blocked.

trees. To solve this issue, we introduce a RIS between the UAV and MR, which aims at enhancing the communication quality. The geometry-based stochastic models (GBSMs) provide a mathematical description of the underlying propagation environments by exploiting available geometrical information and have been widely used in standardized channel models [23]. The proposed wideband channel model also follows the GBSM-based approach to describe the multipath propagations between the UAV and MR, in which the UAV and MR are both equipped with 3D positioned omni-directional ULAs with antenna spacings  $\delta_T$  and  $\delta_R$ , respectively. The UAV is moving in the air with speed  $v_T$ , elevation direction  $\eta_T$ , and azimuth direction  $\gamma_T$ , whereas the MR is moving on the ground with speed  $v_R$  and direction  $\gamma_R$ . At the initial instant, that is,  $t = 0$ , we define the projection of the center of UAV's ULA as the origin of the coordinate system, the line connecting the origin and the center of MR's ULA as the  $x$ -axis, the  $z$ -axis is vertical upward, and thus the  $y$ -axis can be obtained based on the right-hand rule. Then, the initial locations of the central points of UAV's ULA, RIS, and MR's ULA can be expressed as  $(0, 0, H_0)$ ,  $(x_I, y_I, z_I)$ , and  $(\xi_R, 0, 0)$ , respectively.

In this paper, we adopt the planar wavefront assumption because the dimensions of the ULAs and RIS are much smaller than the propagation distances [24]. This leads to different antenna elements in the same ULA and different RIS units sharing the same signal direction. As shown in Fig. 2(a), the azimuth and elevation orientation angles of the 3D positioned UAV's ULA are denoted by  $\psi_T$  and  $\phi_T$ , respectively, whereas at the MR, they are denoted by  $\psi_R$  and  $\phi_R$ , respectively. Moreover, we consider the RIS with  $MN$  reflecting units, which is composed of  $M$  columns (counting from left to right) and  $N$  rows (counting from bottom to top), as shown in Fig. 2(b). The size of each unit, that is,  $d_M \times d_N$ , is usually of sub-wavelength scale, typically ranging from 1/10 to 1/2 of the wavelength, while the gaps between two adjacent units are generally much smaller than the dimension of the unit, and hence are ignored in the following discussions [16]. The existing literature generally assumed the RIS surface being perpendicular to the ground and do not consider the orientations of RIS, which, in principle, will limit the scope of the models. To address this limitation, we introduce a horizontal rotation angle  $\theta_I$  and a vertical rotation angle  $\epsilon_I$  to describe the practical orientations of RIS, which enhances the generality of the proposed channel model and boosts

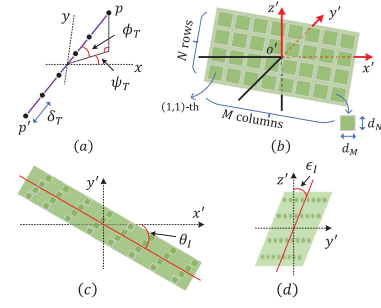


Fig. 2. Definitions of the 3D orientation angles. (a) orientation angles of UAV/MR ULAs; (b) 3D view of RIS; (c) horizontal rotation angle of RIS; (d) vertical rotation angle of RIS.

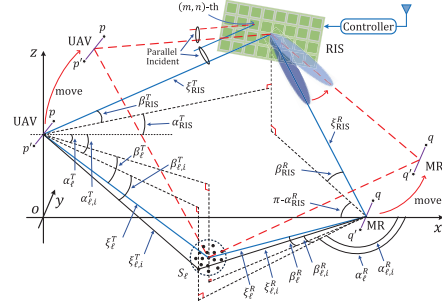


Fig. 3. A visualized illustration of the proposed RIS-assisted UAV channel model. For clarity, only cluster  $S_\ell$  is shown.

the accuracy of the proposed channel model to describe the realistic RIS auxiliary communication systems, as shown in Fig. 2(b)-(d). The three axes in the local coordinate system  $x'-y'-z'$  in Fig. 2(b) are parallel to those in the global coordinate system  $x-y-z$  in Fig. 1. The orientations of the UAV's and MR's ULAs are fixed, whereas the orientation of RIS can be optimized to meet the requirements in different communication conditions, which, in reality, is out of the scope of this paper and will be considered as a future work.

It has been shown in [25] that the channel shows sparsity in high frequency communications, especially for mmWave bands, which indicates that the received signal power concentrates on several main directions with relatively small angular spread when arriving at the MR. Then, we adopt the cluster structure to model the multipath scattering environments between the UAV and ground MR, where each cluster consisting of many scatterers accounts for a distinguishable path with resolvable delay, while the scatterers in the same cluster share similar distances as well as angles and hence result in indistinguishable rays with unresolvable delays [21]. In this paper, we only consider single reflection clusters as have been done in most of the existing literature. Channel models that consider multiple reflection clusters have been described in our previous paper [26]. In the proposed wideband channel model, we assume that there exist  $L$  clusters with resolvable delays, in which the  $\ell$ -th ( $\ell = 1, 2, \dots, L$ ) cluster is denoted by  $S_\ell$ . The definitions of the key model parameters are depicted in Fig. 3 and summarized in Table I. In general, the end-to-end channel propagation statistics between the UAV and MR are of interest in wireless system performance analysis and algorithm validations. Meanwhile, for the signal component that from UAV to MR through RIS, the RIS unit



TABLE I  
SUMMARY OF KEY PARAMETERS DEFINITIONS

$\xi_{\text{RIS}}^T(t), \xi_{\text{RIS}}^R(t)$	distances between UAV/MR and RIS
$\xi_\ell^T(t), \xi_\ell^R(t)$	distances between UAV/MR and cluster $S_\ell$
$\xi_{\ell,i}^T(t), \xi_{\ell,i}^R(t)$	distances between UAV/MR and $S_\ell$ via the $i$ -th ray
$\alpha_{\text{RIS}}^T(t), \beta_{\text{RIS}}^T(t)$	AAoD and EAoD from UAV to RIS
$\alpha_{\text{RIS}}^R(t), \beta_{\text{RIS}}^R(t)$	AAoA and EAoA from RIS to MR
$\alpha_\ell^T(t), \beta_\ell^T(t)$	AAoD and EAoD from UAV to $S_\ell$
$\alpha_{\ell,i}^T(t), \beta_{\ell,i}^T(t)$	AAoD and EAoD from UAV to $S_\ell$ via the $i$ -th ray
$\alpha_\ell^R(t), \beta_\ell^R(t)$	AAoA and EAoA from $S_\ell$ to MR
$\alpha_{\ell,i}^R(t), \beta_{\ell,i}^R(t)$	AAoA and EAoA from $S_\ell$ to MR via the $i$ -th ray
$v_T, \gamma_T, \eta_T$	moving speed and azimuth/elevation directions of UAV
$v_R, \gamma_R$	moving speed and azimuth direction of MR
$\theta_I, \epsilon_I$	vertical and horizontal rotation angles of RIS
$\alpha_{\text{in}}(t), \beta_{\text{in}}(t)$	azimuth and normal incident angles from UAV to RIS
$\alpha_{\text{out}}(t), \beta_{\text{out}}(t)$	azimuth and normal reflected angles from RIS to MR

will manipulate the waves by attaching an additional reflection coefficient, that is, the amplitude  $\chi_{mn}(t)$  and phase  $\varphi_{mn}(t)$ , during the interaction. This process is similar to the waves being reflected/scattered by the scatterers in the cluster. The major difference is that the reflection coefficients of the RIS units are programmable and deterministic, whereas those of the scatterers are random. In light of this, we model the RIS by a *virtual cluster* and RIS units by *virtual scatterers*, which means the rays reflected by different RIS units have similar propagation distances as well as angles and hence are indistinct. Then, we can derive and express the end-to-end complex CIR of the propagation that takes place via the RIS in a similar way as those of the NLoS components as have been done in [27] and [28]. Considering that the UAV and RIS are generally deployed at a relatively higher altitude to provide a broader coverage, and the RIS has the ability to perform passive beamforming, we only take into account the LoS propagation between RIS and UAV/MR.

#### A. Power Scaling Factor of the RIS Component

To study the power delivering capability of RIS, we assume that the UAV antenna array perform beamforming and the MR antenna array perform combining, respectively, so that the transmit and receive ULAs can be both regarded as point sources at the RIS side. We describe the power delivering capability of RIS by power scaling factor  $\Omega_{\text{RIS}}(t)$ , which is defined as the power gain of RIS propagation component relative to the same-distance free path and will be further used to derive the channel response in subsection II.B. Then, we derive Theorem 1.

*Theorem 1: In RIS auxiliary UAV communications, the power scaling factor is given by*

$$\Omega_{\text{RIS}}(t) = \frac{d_M d_N \cos \beta_{\text{in}}(t) (\xi_{\text{RIS}}^T(t) + \xi_{\text{RIS}}^R(t))^2}{4\pi} \times \left| \sum_{m=1}^M \sum_{n=1}^N \frac{\chi_{mn}(t) e^{j(\varphi_{mn}(t) - \varphi_{mn}^{\text{dis}}(t))}}{\xi_{mn}^T(t) \xi_{mn}^R(t)} \right|^2, \quad (1)$$

where  $\varphi_{mn}^{\text{dis}}(t)$  is the distance-related phase term through the  $(m, n)$ -th RIS unit, and  $\beta_{\text{in}}(t) \in [0, \frac{\pi}{2})$  is the incident angle to the normal direction of RIS.

*Proof:* See Appendix A for details. ■

Theorem 1 presents the power scaling factor of RIS component at arbitrary reflection phase configuration, which implies

how the power delivering capability of RIS is affected by the model parameters. Furthermore, it reveals that the incident angle  $\beta_{\text{in}}(t)$  has a great impact on the received power, which has not been explicitly studied in the existing literature. Generally, a smaller incident angle corresponds to a larger reflection aperture, thus more power is reflected and forwarded to the MR. The received signal power can be significantly enhanced when the phases of the received waves from different RIS units are aligned, which can be achieved by performing passive beamforming at the RIS. Then, we have Corollary 1.

*Corollary 1: The optimal reflection phase of the  $(m, n)$ -th RIS unit for achieving a perfect beam aligning towards the MR under non-stationary propagation channels is given by*

$$\begin{aligned} \varphi_{mn}^{\text{opt}}(t) &= \varphi_{\text{RIS}} \\ &\quad - \frac{2\pi}{\lambda} k_M d_M (\sin \beta_{\text{in}}(t) \cos \alpha_{\text{in}}(t) + \sin \beta_{\text{out}}(t) \cos \alpha_{\text{out}}(t)) \\ &\quad - \frac{2\pi}{\lambda} k_N d_N (\sin \beta_{\text{in}}(t) \sin \alpha_{\text{in}}(t) + \sin \beta_{\text{out}}(t) \sin \alpha_{\text{out}}(t)), \end{aligned} \quad (2)$$

where  $\varphi_{\text{RIS}}$  is a controllable phase term that is independent of indexes  $m$  and  $n$ .

*Proof:* With the generalized law of reflection [29] and Theorem 1, Corollary 1 holds when  $\varphi_{mn}(t)$  is configured to offset the phase difference of different units, i.e.,  $\varphi_{mn}^{\text{opt}}(t) = \varphi_{mn}^{\text{dis}}(t)$ . ■

Corollary 1 indicates how the optimal reflection phases of RIS units are affected by the model parameters. Generally,  $\varphi_{\text{RIS}}$  can be set as zero for simplicity. When multiple RISs are deployed,  $\varphi_{\text{RIS}}$  in different RISs should be properly configured to ensure the signals from different RISs to be coherently superimposed at the MR. Furthermore, the power scaling factor  $\Omega_{\text{RIS}}(t)$  in (1) and optimal reflection phase  $\varphi_{mn}^{\text{opt}}(t)$  in (2) are both time-varying due to the motion of UAV and MR, which is different from those in conventional models with constant values. A more detailed discussion on the value of  $\varphi_{mn}(t)$  will be presented in Section IV.

Alternatively, without considering time evolution, we assume that the material-related loss can be neglected, i.e.,  $\chi_{mn} = 1$ , and assume that RIS reflection phase can be continuously and perfectly programmed, that is,  $\varphi_{mn} = \varphi_{mn}^{\text{opt}}$ . By approximating  $\xi_{mn}^T$  and  $\xi_{mn}^R$  with  $\xi_{\text{RIS}}^T$  and  $\xi_{\text{RIS}}^R$ , respectively, we express the power scaling factor under optimal reflection phase configuration as

$$\Omega_{\text{RIS}}^{\text{opt}} \approx \frac{M^2 N^2 d_M d_N \cos \beta_{\text{in}} (\xi_{\text{RIS}}^T + \xi_{\text{RIS}}^R)^2}{4\pi \xi_{\text{RIS}}^T \xi_{\text{RIS}}^R}. \quad (3)$$

Formula (3) indicates that the  $\Omega_{\text{RIS}}^{\text{opt}}$  follows a squaring law with respect to the total number of RIS units  $MN$ , which meets with the results in [30]. Moreover, (3) implies that the relative distance between RIS and UAV/MR can also affect the received power even when the total propagation distance  $\xi_{\text{RIS}}^T + \xi_{\text{RIS}}^R$  is fixed. Let  $\xi_{\text{RIS}}^{\text{TR}} = \xi_{\text{RIS}}^T + \xi_{\text{RIS}}^R$  and  $f(\xi_{\text{RIS}}^{\text{TR}}) = \left( \frac{\xi_{\text{RIS}}^{\text{TR}}}{(\xi_{\text{RIS}}^{\text{TR}} - \xi_{\text{RIS}}^T) \xi_{\text{RIS}}^T} \right)^2$ , by taking the first order derivative with respect to  $\xi_{\text{RIS}}^{\text{TR}}$ , we can show that  $f(\xi_{\text{RIS}}^{\text{TR}})$  is concave and

its minimum value occurs at  $\xi_{\text{RIS}}^T = \xi_{\text{RIS}}^{TR}/2$ . That is to say, we generally prefer to deploy the RIS closer to the UAV or MR instead of at the medium position so as to gain a larger received power. Overall, Eq. (3) embodies guidelines on the practical design and deployment of RIS to achieve higher power gains. Generally, more units, larger unit size, smaller incident angle, shorter end-to-end propagation distance, or closer location to the terminals can cause larger power gains of the RIS component, and hence higher data rate of the system.

### B. Complex CIR of the Proposed Channel Model

The complex channel impulse response (CIR) of the proposed channel model can be characterized by a matrix of size  $M_R \times M_T$ , that is,  $\mathbf{H}(t, \tau, \Theta_T, \Theta_R) = [h_{pq}(t, \tau, \Theta_T, \Theta_R)]_{M_R \times M_T}$ , where  $t$  indicates moving time,  $\tau$  stands for the propagation delay, and  $\Theta_T$  and  $\Theta_R$  denote the departure angle (azimuth angle of departure (AAoD) and elevation angle of departure (EAoD)) and arrival angle (azimuth angle of arrival (AAoA) and elevation angle of arrival (EAoA)) pair of the path, respectively. The  $h_{pq}(t, \tau, \Theta_T, \Theta_R)$  denotes the complex CIR between the  $(p \rightarrow q)$ -th transmit-receive antenna pair, which can be expressed as [25]

$$\begin{aligned} h_{pq}(t, \tau, \Theta_T, \Theta_R) &= h_{pq}^{\text{RIS}}(t) \delta(\tau - \tau_{\text{RIS}}(t)) \delta(\Theta_T - \Theta_T(\alpha_{\text{RIS}}^T(t), \beta_{\text{RIS}}^T(t))) \\ &\quad \times \delta(\Theta_R - \Theta_R(\alpha_{\text{RIS}}^R(t), \beta_{\text{RIS}}^R(t))) \\ &\quad + \sum_{\ell=1}^L h_{\ell,pq}(t) \delta(\tau - \tau_{\ell}(t)) \delta(\Theta_T - \Theta_T(\alpha_{\ell}^T(t), \beta_{\ell}^T(t))) \\ &\quad \times \delta(\Theta_R - \Theta_R(\alpha_{\ell}^R(t), \beta_{\ell}^R(t))), \end{aligned} \quad (4)$$

where  $\tau_{\text{RIS}}(t) = (\xi_{\text{RIS}}^T(t) + \xi_{\text{RIS}}^R(t))/c$  denotes the propagation delay from UAV to MR through RIS,  $(\xi_{\ell}^T(t) + \xi_{\ell}^R(t))/c$  is the propagation delay from UAV to MR via cluster  $S_{\ell}$ , and  $c = 3.0 \times 10^8$  m/s is the speed of light. In (4), the angle pair  $\Theta_T$  and  $\Theta_R$  are expressed in  $\delta(\cdot)$  functions indicating that the channel response only exists in specific departure  $\Theta_T(\alpha_{\text{RIS}}^T(t), \beta_{\text{RIS}}^T(t))$  and arrival  $\Theta_R(\alpha_{\text{RIS}}^R(t), \beta_{\text{RIS}}^R(t))$  angle pairs, which characterize the sparsity of the mmWave channels [25]. Furthermore,  $h_{pq}^{\text{RIS}}(t)$  and  $h_{\ell,pq}(t)$  denote the channel coefficients of the RIS component and NLoS component via cluster  $S_{\ell}$ , respectively. We consider an end-to-end expression of  $h_{pq}^{\text{RIS}}(t)$  by incorporating the RIS power scaling factor, which is different from the existing literatures that interpret  $h_{pq}^{\text{RIS}}(t)$  into two cascaded sub-channels [17]-[19]. In this case,  $h_{pq}^{\text{RIS}}(t)$  and  $h_{\ell,pq}(t)$  can be respectively expressed as

$$\begin{aligned} h_{pq}^{\text{RIS}}(t) &= \sqrt{\frac{\Omega_{\text{RIS}}^{\text{opt}}(t)}{M^2 N^2}} \sum_{m=1}^M \sum_{n=1}^N \chi_{mn}(t) e^{j(\varphi_{mn}(t) - \frac{2\pi}{\lambda}(\xi_{\text{RIS}}^T(t) + \xi_{\text{RIS}}^R(t)))} \\ &\quad \times e^{j\frac{2\pi}{\lambda}k_p \delta_T} \left( \cos(\alpha_{\text{RIS}}^T(t) - \psi_T) \cos \beta_{\text{RIS}}^T(t) \cos \phi_T + \sin \beta_{\text{RIS}}^T(t) \sin \phi_T \right) \\ &\quad \times e^{j\frac{2\pi}{\lambda}k_q \delta_R} \left( \cos(\alpha_{\text{RIS}}^R(t) - \psi_R) \cos \beta_{\text{RIS}}^R(t) \cos \phi_R + \sin \beta_{\text{RIS}}^R(t) \sin \phi_R \right) \end{aligned}$$

$$\begin{aligned} &\times e^{j\frac{2\pi}{\lambda}k_m d_M} \left( \sin \beta_{\text{in}}(t) \cos \alpha_{\text{in}}(t) + \sin \beta_{\text{out}}(t) \cos \alpha_{\text{out}}(t) \right) \\ &\times e^{j\frac{2\pi}{\lambda}k_n d_N} \left( \sin \beta_{\text{in}}(t) \sin \alpha_{\text{in}}(t) + \sin \beta_{\text{out}}(t) \sin \alpha_{\text{out}}(t) \right) \\ &\times e^{j\frac{2\pi}{\lambda}v_T t} \left( \cos(\alpha_{\text{RIS}}^T(t) - \gamma_T) \cos \beta_{\text{RIS}}^T(t) \cos \eta_T + \sin \beta_{\text{RIS}}^T(t) \sin \eta_T \right) \\ &\times e^{j\frac{2\pi}{\lambda}v_R t} \cos(\alpha_{\text{RIS}}^R(t) - \gamma_R) \cos \beta_{\text{RIS}}^R(t), \end{aligned} \quad (5)$$

$$\begin{aligned} h_{\ell,pq}(t) &= \sqrt{\frac{P_{\ell}(t)}{I}} \sum_{i=1}^I e^{j(\varphi_{\ell,i} - \frac{2\pi}{\lambda}(\xi_{\ell,i}^T(t) + \xi_{\ell,i}^R(t)))} \\ &\times e^{j\frac{2\pi}{\lambda}k_p \delta_T} \left( \cos(\alpha_{\ell,i}^T(t) - \psi_T) \cos \beta_{\ell,i}^T(t) \cos \phi_T + \sin \beta_{\ell,i}^T(t) \sin \phi_T \right) \\ &\times e^{j\frac{2\pi}{\lambda}k_q \delta_R} \left( \cos(\alpha_{\ell,i}^R(t) - \psi_R) \cos \beta_{\ell,i}^R(t) \cos \phi_R + \sin \beta_{\ell,i}^R(t) \sin \phi_R \right) \\ &\times e^{j\frac{2\pi}{\lambda}v_T t} \left( \cos(\alpha_{\ell,i}^T(t) - \gamma_T) \cos \beta_{\ell,i}^T(t) \cos \eta_T + \sin \beta_{\ell,i}^T(t) \sin \eta_T \right) \\ &\times e^{j\frac{2\pi}{\lambda}v_R t} \cos(\alpha_{\ell,i}^R(t) - \gamma_R) \cos \beta_{\ell,i}^R(t), \end{aligned} \quad (6)$$

where  $k_p = \frac{M_T - 2p + 1}{2}$  and  $k_q = \frac{M_R - 2q + 1}{2}$ ,  $\lambda$  is the wavelength,  $I$  is the number of rays in cluster  $S_{\ell}$ , and  $P_{\ell}(t)$  denotes the cluster power [31]. Moreover,  $\{\varphi_{\ell,i}\}_{i=1,\dots,I}^{\ell=1,\dots,L}$  are assumed to be independent and uniformly distributed random phases, that is,  $\varphi_{\ell,i} \sim \mathcal{U}[-\pi, \pi)$ .

For the RIS component  $h_{pq}^{\text{RIS}}(t)$ , the initial distance/angular/delay parameters can be determined once the geometric setup among UAV, RIS, and MR is confirmed. For the cluster scattered components  $h_{\ell,pq}(t)$ , we assume that the initial distance/angular/delay parameters can be obtained from a measurement campaign or generated randomly [22], [25]. Then, the values of these aforementioned parameters at time  $t$  can be derived by exploiting the geometric relationships among the UAV, MR, and RIS/clusters based on the initial parameters and the moving speeds/directions/time of the UAV and MR. Therefore, the time-varying distances from the centers of the UAV and MR antenna arrays to the center of RIS can be respectively calculated as

$$\begin{aligned} \xi_{\text{RIS}}^T(t) &= \{(x_I - r_T^x(t))^2 + (y_I - r_T^y(t))^2 \\ &\quad + (z_I - H_0 - r_T^z(t))^2\}^{1/2}, \end{aligned} \quad (7)$$

$$\begin{aligned} \xi_{\text{RIS}}^R(t) &= \{(x_I - \xi_R - r_R^x(t))^2 + (y_I - r_R^y(t))^2 \\ &\quad + (z_I - r_R^z(t))^2\}^{1/2}, \end{aligned} \quad (8)$$

and the corresponding time-varying angles can be expressed as

$$\beta_{\text{RIS}}^R(t) = \arcsin \{z_I / \xi_{\text{RIS}}^R(t)\}, \quad (9)$$

$$\beta_{\text{RIS}}^T(t) = \arcsin \{(z_I - H_0 - v_T t \sin \eta_T) / \xi_{\text{RIS}}^T(t)\}, \quad (10)$$

$$\alpha_{\text{RIS}}^T(t) = \arccos \frac{x_I - v_T t \cos \eta_T \cos \gamma_T}{\sqrt{(x_I - r_T^x(t))^2 + (y_I - r_T^y(t))^2}}, \quad (11)$$

$$\alpha_{\text{RIS}}^R(t) = \arccos \frac{x_I - \xi_R - v_R t \cos \gamma_R}{\sqrt{(x_I - \xi_R - r_R^x(t))^2 + (y_I - r_R^y(t))^2}}. \quad (12)$$

Moreover, the time-varying distances from the centers of UAV and MR antenna arrays to cluster  $S_{\ell}$ , denoted by  $\xi_{\ell}^T(t)$  and  $\xi_{\ell}^R(t)$ , respectively, and those from the centers of UAV and

MR antenna arrays to cluster  $S_\ell$  via the  $i$ -th ray, they are,  $\xi_{\ell,i}^T(t)$  and  $\xi_{\ell,i}^R(t)$ , respectively, can be calculated as

$$\xi_\ell^R(t) = \{(\xi_{R,\ell}^x(0) - r_R^x(t))^2 + (\xi_{R,\ell}^y(0) - r_R^y(t))^2 + (\xi_{R,\ell}^z(0) - r_R^z(t))^2\}^{1/2}, \quad (13)$$

$$\xi_{\ell,i}^R(t) = \{(\xi_{R,\ell,i}^x(0) - r_R^x(t))^2 + (\xi_{R,\ell,i}^y(0) - r_R^y(t))^2 + (\xi_{R,\ell,i}^z(0) - r_R^z(t))^2\}^{1/2}, \quad (14)$$

$$\xi_\ell^T(t) = \{(\xi_R + \xi_{R,\ell}^x(0) - r_T^x(t))^2 + (\xi_{R,\ell}^y(0) - r_T^y(t))^2 + (\xi_{R,\ell}^z(0) - H_0 - r_T^z(t))^2\}^{1/2}, \quad (15)$$

$$\xi_{\ell,i}^T(t) = \{(\xi_R + \xi_{R,\ell,i}^x(0) - r_T^x(t))^2 + (\xi_{R,\ell,i}^y(0) - r_T^y(t))^2 + (\xi_{R,\ell,i}^z(0) - H_0 - r_T^z(t))^2\}^{1/2}, \quad (16)$$

and the corresponding time-varying ray angles can be expressed as

$$\beta_{\ell,i}^R(t) = \arcsin \{ \xi_\ell^R(0) \sin \beta_{\ell,i}^R(0) / \xi_{\ell,i}^R(t) \}, \quad (17)$$

$$\beta_{\ell,i}^T(t) = \arcsin \{ (\xi_{R,\ell,i}^z(0) - H_0 - r_T^z(t)) / \xi_{\ell,i}^T(t) \}, \quad (18)$$

$$\alpha_{\ell,i}^R(t) = \arccos \frac{\xi_{R,\ell,i}^x(0) - v_R t \cos \gamma_R}{\sqrt{\xi_{\ell,i}^R(t) - (\xi_{R,\ell,i}^z(0) - r_R^z(t))^2}}, \quad (19)$$

$$\alpha_{\ell,i}^T(t) = \arccos \left\{ (\xi_R + \xi_{R,\ell,i}^x(0) - v_T t \cos \eta_T \cos \gamma_T) \times \frac{1}{\sqrt{\xi_{\ell,i}^T(t) - (\xi_{R,\ell,i}^z(0) - H_0 - r_T^z(t))^2}} \right\}, \quad (20)$$

where we apply  $t = 0$  to denote the initial values of these parameters. Moreover,  $r_T^x(t) = v_T t \cos \eta_T \cos \gamma_T$ ,  $r_T^y(t) = v_T t \cos \eta_T \sin \gamma_T$ , and  $r_T^z(t) = v_T t \sin \eta_T$  are the moving displacements of the UAV in the  $x$ ,  $y$ , and  $z$  directions, respectively; while at the MR, they are expressed as  $r_R^x(t) = v_R t \cos \gamma_R$ ,  $r_R^y(t) = v_R t \sin \gamma_R$ , and  $r_R^z(t) = 0$ , respectively. In addition,  $\xi_{R,\ell}^x(0) = \xi_\ell^R(0) \cos \beta_{\ell,i}^R(0) \cos \alpha_{\ell,i}^R(0)$ ,  $\xi_{R,\ell}^y(0) = \xi_\ell^R(0) \cos \beta_{\ell,i}^R(0) \sin \alpha_{\ell,i}^R(0)$ , and  $\xi_{R,\ell}^z(0) = \xi_\ell^R(0) \sin \beta_{\ell,i}^R(0)$  constitute the initial distance vector from MR to cluster  $S_\ell$ , that is,  $[\xi_{R,\ell}^x(0), \xi_{R,\ell}^y(0), \xi_{R,\ell}^z(0)]^T$ ; meanwhile,  $[\xi_{R,\ell,i}^x(0), \xi_{R,\ell,i}^y(0), \xi_{R,\ell,i}^z(0)]^T$  denotes the distance vector from MR to cluster  $S_\ell$  via the  $i$ -th ray, where  $\xi_{R,\ell,i}^x(0) = \xi_\ell^R(0) \cos \beta_{\ell,i}^R(0) \cos \alpha_{\ell,i}^R(0)$ ,  $\xi_{R,\ell,i}^y(0) = \xi_\ell^R(0) \cos \beta_{\ell,i}^R(0) \sin \alpha_{\ell,i}^R(0)$ , and  $\xi_{R,\ell,i}^z(0) = \xi_\ell^R(0) \sin \beta_{\ell,i}^R(0)$ . The derivations of the incident ( $\alpha_{\text{in}}(t), \beta_{\text{in}}(t)$ ) and reflected ( $\alpha_{\text{out}}(t), \beta_{\text{out}}(t)$ ) angles are in Appendix B.

Moreover, the time-varying cluster power  $P_\ell(t)$  is generated by [23]

$$P_\ell(t) = \exp \left( -\tau_\ell(t) \frac{r_\tau - 1}{r_\tau \sigma_\tau} \right) \cdot 10^{\frac{-Z_\ell}{10}}, \quad (21)$$

where  $r_\tau$  is the delay scaling parameter,  $\sigma_\tau$  is the delay spread, and  $Z_\ell$  is a Gaussian distributed random variable, i.e.,  $Z_\ell \sim \mathcal{N}(0, \zeta^2)$ , and their values can be obtained from Table 7.5.6 in [23].

*Corollary 2:* When the physical direct path between UAV and MR is obstructed, the fading of the end-to-end channel  $h_{pq}(t, \tau, \Theta_T, \Theta_R)$  in (4) can be characterized by Rician fading. Moreover, by borrowing the concept of Rice factor

from Rician fading channels, we define the virtual Rice factor of the proposed non-stationary RIS auxiliary UAV mmWave channel model as

$$K^{\text{vir}}(t) = \frac{\Omega_{\text{RIS}}(t)}{\sum_{\ell=1}^L P_\ell(t)}. \quad (22)$$

*Proof:* See Appendix C for details. ■

Corollary 2 reveals that the physical indirect RIS component  $h_{pq}^{\text{RIS}}(t)$  has the ability to provide a deterministic component on the received signals, which behaves similarly to the physical direct LoS component between the UAV and MR, thus we name it the *virtual LoS (V-LoS)* component provided by RIS. Moreover, Corollary 2 provides a new view on the modeling of the channel statistics in RIS auxiliary communication systems by considering the end-to-end propagation channel between the transceivers, which is distinguishable from the results in [17]–[19].

In this paper, we mainly focus on the small-scale fading characterization of the RIS auxiliary MIMO UAV-to-ground mmWave communication channels. We normalize the power of the complex CIR  $h_{pq}(t, \tau, \Theta_T, \Theta_R)$  to one, to provide a general representation, as [23]

$$\begin{aligned} h_{pq}^{\text{RIS}}(t) &= \sqrt{\frac{K^{\text{vir}}(t)}{(K^{\text{vir}}(t) + 1) |\Upsilon(t)|^2}} \\ &\times \sum_{m=1}^M \sum_{n=1}^N \chi_{mn}(t) e^{j(\varphi_{mn}(t) - \frac{2\pi}{\lambda} (\xi_{\text{RIS}}^T(t) + \xi_{\text{RIS}}^R(t)))} \\ &\times e^{j \frac{2\pi}{\lambda} k_p \delta_T (\cos(\alpha_{\text{RIS}}^T(t) - \psi_T) \cos \beta_{\text{RIS}}^T(t) \cos \phi_T + \sin \beta_{\text{RIS}}^T(t) \sin \phi_T)} \\ &\times e^{j \frac{2\pi}{\lambda} k_q \delta_R (\cos(\alpha_{\text{RIS}}^R(t) - \psi_R) \cos \beta_{\text{RIS}}^R(t) \cos \phi_R + \sin \beta_{\text{RIS}}^R(t) \sin \phi_R)} \\ &\times e^{j \frac{2\pi}{\lambda} k_m d_M (\sin \beta_{\text{in}}(t) \cos \alpha_{\text{in}}(t) + \sin \beta_{\text{out}}(t) \cos \alpha_{\text{out}}(t))} \\ &\times e^{j \frac{2\pi}{\lambda} k_n d_N (\sin \beta_{\text{in}}(t) \sin \alpha_{\text{in}}(t) + \sin \beta_{\text{out}}(t) \sin \alpha_{\text{out}}(t))} \\ &\times e^{j \frac{2\pi}{\lambda} v_T t (\cos(\alpha_{\text{RIS}}^T(t) - \gamma_T) \cos \beta_{\text{RIS}}^T(t) \cos \eta_T + \sin \beta_{\text{RIS}}^T(t) \sin \eta_T)} \\ &\times e^{j \frac{2\pi}{\lambda} v_R t \cos(\alpha_{\text{RIS}}^R(t) - \gamma_R) \cos \beta_{\text{RIS}}^R(t)}, \end{aligned} \quad (23)$$

$$\begin{aligned} h_{\ell,pq}(t) &= \sqrt{\frac{P'_\ell(t)}{(K^{\text{vir}}(t) + 1) I}} \sum_{i=1}^I e^{j(\varphi_{\ell,i}(t) - \frac{2\pi}{\lambda} (\xi_{\ell,i}^T(t) + \xi_{\ell,i}^R(t)))} \\ &\times e^{j \frac{2\pi}{\lambda} k_p \delta_T (\cos(\alpha_{\ell,i}^T(t) - \psi_T) \cos \beta_{\ell,i}^T(t) \cos \phi_T + \sin \beta_{\ell,i}^T(t) \sin \phi_T)} \\ &\times e^{j \frac{2\pi}{\lambda} k_q \delta_R (\cos(\alpha_{\ell,i}^R(t) - \psi_R) \cos \beta_{\ell,i}^R(t) \cos \phi_R + \sin \beta_{\ell,i}^R(t) \sin \phi_R)} \\ &\times e^{j \frac{2\pi}{\lambda} v_T t (\cos(\alpha_{\ell,i}^T(t) - \gamma_T) \cos \beta_{\ell,i}^T(t) \cos \eta_T + \sin \beta_{\ell,i}^T(t) \sin \eta_T)} \\ &\times e^{j \frac{2\pi}{\lambda} v_R t \cos(\alpha_{\ell,i}^R(t) - \gamma_R) \cos \beta_{\ell,i}^R(t)}, \end{aligned} \quad (24)$$

where  $\Upsilon(t) = \sum_{m=1}^M \sum_{n=1}^N \chi_{mn}(t) e^{j(\varphi_{mn}(t) - \varphi_{mn}^{\text{dis}}(t))}$ . The  $P'_\ell(t) = P_\ell(t) / \sum_{\ell=1}^L P_\ell(t)$  is the normalized power ratio of the clusters [31]. The  $\varphi_{mn}(t)$  in (23) stands for the programmable RIS reflection phase, whose optimal value is given in Corollary 1. Consequently, Eqs.(23)-(24) provide a generalized



description of the end-to-end physical properties of RIS auxiliary UAV-to-ground mmWave communication channels, which effectively reveals the programmability of the channels owing to the presence of RIS and is different from conventional cascaded channel models in [17]–[19]. The proposed 3D modeling approach in this paper is a general channel modeling method that is suitable for various kinds of RIS-assisted UAV-to-ground communication scenarios. Specifically, by replacing the antenna steering vectors expressions of the ULAs in lines 2-3 of Eqs. (5)-(6) and (23)-(24) with those of the uniform circular arrays (UCAs) or uniform planar arrays (UPAs), the proposed channel model can be adapted to describe the condition that the UAV and MR are equipped with UCAs or UPAs. Alternatively, when we ignore the time evolution of the model parameters, the proposed channel model can be used to describe stationary channel; when we set cluster number  $L$  as one, it can be used to describe narrowband channel; and when we set the RIS component  $h_{pq}^{\text{RIS}}(t)$  as zero, it reduces to be conventional Rayleigh fading channel without RIS. This shows the generality of the proposed channel model.

### III. STATISTICAL PROPERTIES OF THE PROPOSED CHANNEL MODEL

#### A. Fading Characteristic

In conventional no-RIS auxiliary UAV mmWave communication system, the fading of the end-to-end propagation channel between the transceiver is characterized by Rayleigh fading when the direct path is blocked. This can be derived from the proposed channel model by setting the RIS component  $h_{pq}^{\text{RIS}}(t)$  in (4) as zero. Then, by introducing a RIS between the UAV and MR, Corollary 2 has shown that the fading of the proposed RIS auxiliary channel can be characterized by Rician fading with virtual Rice factor  $K^{\text{vir}}(t)$  and envelope power  $\Omega_{\text{RIS}}(t) + \sum_{\ell=1}^L P_{\ell}(t)$ .

When the RIS controller applies the random reflection phase configuration in each unit, on the other hand, the reflection phase  $\varphi_{mn}(t)$  becomes a random variable, and hence the RIS component  $h_{pq}^{\text{RIS}}(t)$  becomes a random process. In this case, the fading of the end-to-end RIS auxiliary channel depends on the reflection phase controlling mechanism as well as the total unit number, and cannot be characterized by Rician fading. An example is that when the controller applies random uniform reflection phase configuration, that is,  $\varphi_{mn}(t) \sim \mathcal{U}[-\pi, \pi)$ , and the unit number  $MN$  is large enough,  $h_{pq}(t, \tau, \mathbf{\Theta}_T, \mathbf{\Theta}_R)$  can be characterized by Rayleigh fading with envelope power  $\mathbb{E}[\Omega_{\text{RIS}}(t)] + \sum_{\ell=1}^L P_{\ell}(t)$  based on the Central Limit Theorem.

#### B. Time-Varying Spatial-Temporal (ST) Cross-Correlation Function (CCF)

As shown in [22], [32], the local correlation properties of a channel are determined by the correlation properties between  $h_{pq}(t)$  and  $h_{p'q'}(t + \Delta t)$  in each tap; meanwhile, it is generally assumed that there is no correlation between different clusters. Therefore, the normalized time-varying ST

CCF of the proposed channel model can be defined as [22]

$$\rho_{(p,q),(p',q')}(t, \Delta p, \Delta q, \Delta t) = \frac{\mathbb{E}[h_{pq}^*(t)h_{p'q'}(t + \Delta t)]}{\sqrt{\mathbb{E}[|h_{pq}(t)|^2]\mathbb{E}[|h_{p'q'}(t + \Delta t)|^2]}}, \quad (25)$$

where  $\Delta t$  is the time difference,  $\Delta p = |k_{p'} - k_p|\delta_T/\lambda$  and  $\Delta q = |k_{q'} - k_q|\delta_R/\lambda$  denote the normalized antenna spacings of the UAV and MR antenna arrays, respectively, and  $p, p', q$ , and  $q'$  are the antenna indexes. In addition,  $h_{pq}(t)$  and  $h_{p'q'}(t + \Delta t)$  denote the complex channel coefficients of the  $(p \rightarrow q)$ -th and  $(p' \rightarrow q')$ -th transmit-receive antenna pairs, respectively.

By substituting (23) and (24) into (25), we obtain the time-varying ST CCF of the proposed channel model as  $\rho_{(p,q),(p',q')}(t, \Delta p, \Delta q, \Delta t) = \rho_{(p,q),(p',q')}^{\text{RIS}}(t, \Delta p, \Delta q, \Delta t) + \rho_{(p,q),(p',q'),\ell}^{\text{NLoS}}(t, \Delta p, \Delta q, \Delta t)$ , in which the  $\rho_{(p,q),(p',q')}^{\text{RIS}}(t, \Delta p, \Delta q, \Delta t)$  and  $\rho_{(p,q),(p',q'),\ell}^{\text{NLoS}}(t, \Delta p, \Delta q, \Delta t)$  denote the local ST CCF of the RIS and NLoS components, respectively. Moreover, by further imposing  $\Delta t = 0$ , we can obtain the following spatial CCF of the RIS component

$$\begin{aligned} & \rho_{(p,q),(p',q')}^{\text{RIS}}(t, \Delta p, \Delta q) \\ &= \frac{K^{\text{vir}}(t)}{K^{\text{vir}}(t) + 1} \\ & \times e^{j2\pi\Delta p \left( \cos(\alpha_{\text{RIS}}^T(t) - \psi_T) \cos \beta_{\text{RIS}}^T(t) \cos \phi_T + \sin \beta_{\text{RIS}}^T(t) \sin \phi_T \right)} \\ & \times e^{j2\pi\Delta q \left( \cos(\alpha_{\text{RIS}}^R(t) - \psi_R) \cos \beta_{\text{RIS}}^R(t) \cos \phi_R + \sin \beta_{\text{RIS}}^R(t) \sin \phi_R \right)}, \end{aligned} \quad (26)$$

and the spatial CCF of the NLoS components

$$\begin{aligned} & \rho_{(p,q),(p',q'),\ell}^{\text{NLoS}}(t, \Delta p, \Delta q) \\ &= \frac{P_{\ell}'(t)}{K^{\text{vir}}(t) + 1} \int_{-\pi}^{\pi} \int_{-\pi}^{\pi} e^{j2\pi\Delta p \cos(\alpha_{\ell}^T(t) - \psi_T) \cos \beta_{\ell}^T(t) \cos \phi_T} \\ & \times e^{j2\pi\Delta p \sin \beta_{\ell}^T(t) \sin \phi_T} \\ & \times e^{j2\pi\Delta q \left( \cos(\alpha_{\ell}^R(t) - \psi_R) \cos \beta_{\ell}^R(t) \cos \phi_R + \sin \beta_{\ell}^R(t) \sin \phi_R \right)} \\ & \times f(\alpha_{\ell}^R, \beta_{\ell}^R) d(\alpha_{\ell}^R, \beta_{\ell}^R), \end{aligned} \quad (27)$$

where  $f(\alpha_{\ell}^R, \beta_{\ell}^R)$  is the joint probability density function (PDF) of the received azimuth  $\alpha_{\ell}^R$  and elevation  $\beta_{\ell}^R$  angles. In general, the arrival angles (AAoA and EAoA) and departure angles (AAoD and EAoD) are dependent on each other when the geometrical setup is confirmed in the proposed single-bounced channel model [22]. In cluster structure, especially for mmWave communications, the directions of the rays in each cluster are generally limited to a certain range. Different kinds of distributions, such as von Mises distribution [33], [34], lognormal distribution [35], Laplace distribution [25], and truncated Gaussian distribution [36], [37], etc., have been adopted for characterizing the ray angle distribution. Specifically, 3GPP adopts the truncated Gaussian distribution in the standard UAV-to-ground channel models [37]. Therefore, we also follow this modeling assumption in this paper. Then, the PDF for the wave with direction  $\vartheta$  being limited within

the interval from  $\vartheta_{\text{low}}$  to  $\vartheta_{\text{up}}$ , i.e.,  $\vartheta \in [\vartheta_{\text{low}}, \vartheta_{\text{up}}]$ , can be expressed as

$$f(\vartheta, \mu_\vartheta, \sigma_\vartheta, \vartheta_{\text{low}}, \vartheta_{\text{up}}) = \frac{\frac{1}{\sigma_\vartheta} u\left(\frac{\vartheta - \mu_\vartheta}{\sigma_\vartheta}\right)}{\Phi\left(\frac{\vartheta_{\text{up}} - \mu_\vartheta}{\sigma_\vartheta}\right) - \Phi\left(\frac{\vartheta_{\text{low}} - \mu_\vartheta}{\sigma_\vartheta}\right)}, \quad (28)$$

where  $\mu_\vartheta$  and  $\sigma_\vartheta$  denote the mean value and angle spread of the signal direction  $\vartheta$ , respectively. In addition,  $u(\varsigma)$  is the PDF of the standard normal distributed random variable  $\varsigma$ , which can be expressed as  $u(\varsigma) = \frac{1}{\sqrt{2\pi}} \exp\{-\frac{\varsigma^2}{2}\}$ , whereas  $\Phi(\varsigma) = \int_{-\infty}^{\varsigma} u(\varsigma') d\varsigma' = \frac{1}{2}(1 + \text{erf}(\frac{\varsigma}{\sqrt{2}}))$  represents the cumulative distribution function (CDF) of the standard normal distributed random variable  $\varsigma$  with  $\text{erf}(\cdot)$  being the Gauss error function. The signal azimuth and elevation angles are generally assumed to be independent of each other, thus the joint PDF in (27) can be derived from (28) as  $f(\alpha_\ell^R, \beta_\ell^R) = f(\alpha_\ell^R, \mu_{\alpha_\ell^R}, \sigma_{\alpha_\ell^R}, \alpha_{\ell,\text{low}}^R, \alpha_{\ell,\text{up}}^R) \cdot f(\beta_\ell^R, \mu_{\beta_\ell^R}, \sigma_{\beta_\ell^R}, \beta_{\ell,\text{low}}^R, \beta_{\ell,\text{up}}^R)$ .

### C. Temporal Auto-Correlation Function (ACF) and Doppler Power Spectral Density (PSD)

The temporal ACF of the proposed channel model can be derived from the ST CCF  $\rho_{(p,q),(p',q')}(t, \Delta p, \Delta q, \Delta t)$  by applying  $\Delta p = \Delta q = 0$ , that is,  $p = p'$  and  $q = q'$ , which is expressed as

$$\rho(t, \Delta t) = \rho^{\text{RIS}}(t, \Delta t) + \rho_\ell^{\text{NLoS}}(t, \Delta t), \quad (29)$$

where  $\rho^{\text{RIS}}(t, \Delta t)$  and  $\rho_\ell^{\text{NLoS}}(t, \Delta t)$  stand for the temporal ACFs of the RIS and NLoS components, respectively, which are expressed as (30) and (31), shown at the bottom of the page, respectively. It is obvious that the temporal ACFs of the proposed channel model depend on time  $t$  and time difference  $\Delta t$ , which reveals the non-stationarity of the channel model. Moreover, (30) indicates that the channel with RIS has the

ability to provide longer channel temporal correlation time than the channel without RIS by appropriately programming the RIS reflection phases  $\varphi_{mn}(t)$ , so that the channel can be less frequently estimated and more saved time can be used for data transmission. This boosts the communication performance.

The Doppler PSD of the proposed channel model is defined as the Fourier transform of temporal ACF  $\rho(t, \Delta t)$  in (29) with respect to time difference  $\Delta t$  [38], that is,

$$S(t, \nu) = \int_{-\infty}^{\infty} \rho(t, \Delta t) e^{-j2\pi\nu\Delta t} d(\Delta t) \\ = S^{\text{RIS}}(t, \nu) + S_\ell^{\text{NLoS}}(t, \nu), \quad (32)$$

where  $\nu$  stands for the Doppler frequency, and  $S^{\text{RIS}}(t, \nu)$  and  $S_\ell^{\text{NLoS}}(t, \nu)$  denote the Doppler PSDs of the RIS and NLoS components, respectively, which are expressed as

$$S^{\text{RIS}}(t, \nu) = \int_{-\infty}^{\infty} \rho^{\text{RIS}}(t, \Delta t) e^{-j2\pi\nu\Delta t} d(\Delta t), \quad (33)$$

$$S_\ell^{\text{NLoS}}(t, \nu) = \int_{-\infty}^{\infty} \rho_\ell^{\text{NLoS}}(t, \Delta t) e^{-j2\pi\nu\Delta t} d(\Delta t). \quad (34)$$

It can be seen that the Doppler PSD of the proposed channel model is related to the moving time  $t$  as well as the moving states (speeds and directions) of the UAV and MR, which is in agreement with the models in [24], [38].

### D. Time-Varying Frequency Correlation Function (FCF) and Power Delay Profile (PDP)

The time-varying transfer function of the proposed channel model is defined as the Fourier transform of the complex CIR  $h_{pq}(t, \tau, \Theta_T, \Theta_R)$  in (4) with respect to the propagation delay

$$\rho^{\text{RIS}}(t, \Delta t) \\ = \sqrt{\frac{K^{\text{vir}}(t)}{K^{\text{vir}}(t) + 1}} \sqrt{\frac{K^{\text{vir}}(t + \Delta t)}{K^{\text{vir}}(t + \Delta t) + 1}} \times \frac{\mathbb{E}[\Upsilon^*(t) \Upsilon(t + \Delta t)]}{\sqrt{\mathbb{E}[\Upsilon(t)^2] \mathbb{E}[\Upsilon(t + \Delta t)^2]}} \times e^{j\frac{2\pi}{\lambda} (\xi_{\text{RIS}}^T(t) - \xi_{\text{RIS}}^T(t + \Delta t) + \xi_{\text{RIS}}^R(t) - \xi_{\text{RIS}}^R(t + \Delta t))} \\ \times e^{j\frac{2\pi}{\lambda} k_p \delta_T \left\{ \cos(\alpha_{\text{RIS}}^T(t + \Delta t) - \psi_T) \cos \beta_{\text{RIS}}^T(t + \Delta t) \cos \phi_T + \sin \beta_{\text{RIS}}^T(t + \Delta t) \sin \phi_T - \left[ \cos(\alpha_{\text{RIS}}^T(t) - \psi_T) \cos \beta_{\text{RIS}}^T(t) \cos \phi_T + \sin \beta_{\text{RIS}}^T(t) \sin \phi_T \right] \right\}} \\ \times e^{j\frac{2\pi}{\lambda} k_q \delta_R \left\{ \cos(\alpha_{\text{RIS}}^R(t + \Delta t) - \psi_R) \cos \beta_{\text{RIS}}^R(t + \Delta t) \cos \phi_R + \sin \beta_{\text{RIS}}^R(t + \Delta t) \sin \phi_R - \left[ \cos(\alpha_{\text{RIS}}^R(t) - \psi_R) \cos \beta_{\text{RIS}}^R(t) \cos \phi_R + \sin \beta_{\text{RIS}}^R(t) \sin \phi_R \right] \right\}} \\ \times e^{j\frac{2\pi}{\lambda} v_T \left\{ (t + \Delta t) \cdot \left[ \cos(\alpha_{\text{RIS}}^T(t + \Delta t) - \gamma_T) \cos \beta_{\text{RIS}}^T(t + \Delta t) \cos \eta_T + \sin \beta_{\text{RIS}}^T(t + \Delta t) \sin \eta_T \right] - t \left[ \cos(\alpha_{\text{RIS}}^T(t) - \gamma_T) \cos \beta_{\text{RIS}}^T(t) \cos \eta_T + \sin \beta_{\text{RIS}}^T(t) \sin \eta_T \right] \right\}} \\ \times e^{j\frac{2\pi}{\lambda} \left[ v_R \cdot (t + \Delta t) \cos(\alpha_{\text{RIS}}^R(t + \Delta t) - \gamma_R) \cos \beta_{\text{RIS}}^R(t + \Delta t) - v_R t \cos(\alpha_{\text{RIS}}^R(t) - \gamma_R) \cos \beta_{\text{RIS}}^R(t) \right]}. \quad (30)$$

$$\rho_\ell^{\text{NLoS}}(t, \Delta t) \\ = \sqrt{\frac{P'_\ell(t)}{K^{\text{vir}}(t) + 1}} \sqrt{\frac{P'_\ell(t + \Delta t)}{K^{\text{vir}}(t + \Delta t) + 1}} \times \frac{1}{I} \sum_{i=1}^I \mathbb{E} \left\{ e^{j\frac{2\pi}{\lambda} (\xi_{\ell,i}^T(t) - \xi_{\ell,i}^T(t + \Delta t) + \xi_{\ell,i}^R(t) - \xi_{\ell,i}^R(t + \Delta t))} \right. \\ \times e^{j\frac{2\pi}{\lambda} k_p \delta_T \left\{ \cos(\alpha_{\ell,i}^T(t + \Delta t) - \psi_T) \cos \beta_{\ell,i}^T(t + \Delta t) \cos \phi_T + \sin \beta_{\ell,i}^T(t + \Delta t) \sin \phi_T - \left[ \cos(\alpha_{\ell,i}^T(t) - \psi_T) \cos \beta_{\ell,i}^T(t) \cos \phi_T + \sin \beta_{\ell,i}^T(t) \sin \phi_T \right] \right\}} \\ \times e^{j\frac{2\pi}{\lambda} k_q \delta_R \left\{ \cos(\alpha_{\ell,i}^R(t + \Delta t) - \psi_R) \cos \beta_{\ell,i}^R(t + \Delta t) \cos \phi_R + \sin \beta_{\ell,i}^R(t + \Delta t) \sin \phi_R - \left[ \cos(\alpha_{\ell,i}^R(t) - \psi_R) \cos \beta_{\ell,i}^R(t) \cos \phi_R + \sin \beta_{\ell,i}^R(t) \sin \phi_R \right] \right\}} \\ \times e^{j\frac{2\pi}{\lambda} v_T \left\{ (t + \Delta t) \cdot \left[ \cos(\alpha_{\ell,i}^T(t + \Delta t) - \gamma_T) \cos \beta_{\ell,i}^T(t + \Delta t) \cos \eta_T + \sin \beta_{\ell,i}^T(t + \Delta t) \sin \eta_T \right] - t \left[ \cos(\alpha_{\ell,i}^T(t) - \gamma_T) \cos \beta_{\ell,i}^T(t) \cos \eta_T + \sin \beta_{\ell,i}^T(t) \sin \eta_T \right] \right\}} \\ \left. \times e^{j\frac{2\pi}{\lambda} \left[ v_R \cdot (t + \Delta t) \cos(\alpha_{\ell,i}^R(t + \Delta t) - \gamma_R) \cos \beta_{\ell,i}^R(t + \Delta t) - v_R t \cos(\alpha_{\ell,i}^R(t) - \gamma_R) \cos \beta_{\ell,i}^R(t) \right] \right\}. \quad (31)$$



$\tau$ , which is expressed as

$$H_{pq}(t, f) = h_{pq}^{\text{RIS}}(t) e^{-j2\pi f \tau^{\text{RIS}}(t)} + \sum_{\ell=1}^L h_{\ell, pq}(t) e^{-j2\pi f \tau_{\ell}(t)}. \quad (35)$$

Thus, the normalized FCF of the proposed channel model can be defined as [36]

$$\rho_{H_{pq}}(t, \Delta f) = \frac{\mathbb{E}[H_{pq}^*(t, f) H_{pq}(t, f + \Delta f)]}{\sqrt{\mathbb{E}[|H_{pq}(t, f)|^2] \mathbb{E}[|H_{pq}(t, f + \Delta f)|^2]}}, \quad (36)$$

where  $\Delta f$  denotes frequency separation. With the uncorrelated scattering (US) assumption [32], the substitution of (23), (24), and (35) into (36) yields the following FCF

$$\rho_{H_{pq}}(t, \Delta f) = \frac{K^{\text{vir}}(t)}{K^{\text{vir}}(t) + 1} e^{-j2\pi \Delta f \tau^{\text{RIS}}(t)} + \frac{1}{K^{\text{vir}}(t) + 1} \sum_{\ell=1}^L P'_{\ell}(t) e^{-j2\pi \Delta f \tau_{\ell}(t)}. \quad (37)$$

By applying inverse Fourier transform to the FCF  $\rho_{H_{pq}}(t, \Delta f)$  with respect to frequency separation  $\Delta f$ , we can further derive the PDP of the proposed channel model as

$$S_{H_{pq}}(t, \tau) = \frac{K^{\text{vir}}(t)}{K^{\text{vir}}(t) + 1} \delta(\tau - \tau^{\text{RIS}}(t)) + \frac{1}{K^{\text{vir}}(t) + 1} \sum_{\ell=1}^L P'_{\ell}(t) \delta(\tau - \tau_{\ell}(t)). \quad (38)$$

The FCF and PDP of the proposed channel model are related to moving time  $t$  but independent of frequency  $f$ , which indicates that the channel model is non-stationary in time domain but stationary in frequency domain. Moreover, it implies that the RIS reflection phase configuration will also affect the FCF and PDP through the power scaling factor, which is a specific feature of the RIS auxiliary communication channels.

#### IV. RESULTS AND DISCUSSIONS

In this section, we numerically study the channel characteristics of the proposed channel model by comparing the theoretical results with simulated as well as measurement results.

##### A. Simulation Setup

The proposed channel model is operated at a carrier frequency of  $f_c = 28$  GHz. The parameters used in the simulations are listed here or specified otherwise:  $M_T = 4$ ,  $M_R = 6$ ,  $\xi_R = 100$  m,  $H_0 = 50$  m,  $\chi_{mn} = 1$ ,  $\delta_T = \delta_R = \lambda/2$ ,  $\psi_T = \pi/3$ ,  $\phi_T = \pi/4$ ,  $\psi_R = \pi/4$ ,  $\phi_R = \pi/4$ ,  $\xi_{\ell}^R(0) = 60$  m,  $\mu_{\alpha_{\ell}^R} = 2\pi/3$ ,  $\sigma_{\alpha_{\ell}^R} = \pi/18$ ,  $\mu_{\beta_{\ell}^R} = \pi/4$ , and  $\sigma_{\beta_{\ell}^R} = \pi/18$  [25], [36]. Two kinds of configurations of RIS with  $MN = 4 \times 10^4$  are considered, that is, RIS<sub>A</sub> with strip configuration  $M = 400, N = 100$  and RIS<sub>B</sub> with square configuration  $M = N = 200$ . The RIS is located at  $(x_I, y_I, z_I) = (70$  m, 30 m, 15 m) with the rotation angles  $\theta_I = -\pi/18$  and  $\epsilon_I = -\pi/18$ , and the size of the RIS unit is set as  $d_M = d_N = \lambda/4$ . Finally, the moving speed and

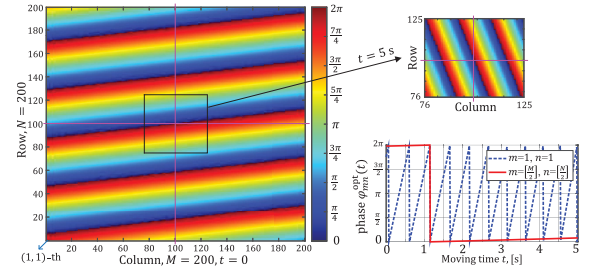


Fig. 4. Normalized reflection phases of RIS under optimal reflection phase configuration.

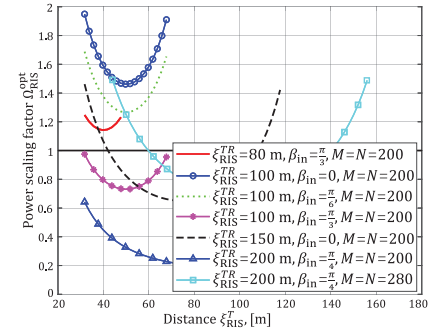


Fig. 5. Power scaling factor  $\Omega_{\text{RIS}}^{\text{opt}}$  of the RIS component under optimal reflection phase configuration.

direction of the UAV are set as  $v_T = 5$  m/s,  $\gamma_T = 0$  in azimuth direction and  $\eta_T = 0$  in elevation direction, respectively, whereas at MR they are set as  $v_R = 2$  m/s and  $\gamma_R = 0$ .

Moreover, the impacts of different RIS reflection phase configurations are evaluated, where

i) *Optimal*: The RIS controller applies optimal reflection phase configuration with  $\varphi_{mn}(t) = \varphi_{mn}^{\text{opt}}(t)$ . In this case,  $\Omega_{\text{RIS}}(t) = \Omega_{\text{RIS}}^{\text{opt}}(t)$  and the channel is characterized by Rician fading.

ii) *Discrete*: The RIS controller applies discrete reflection phase configuration with  $\varphi_{mn}(t) = \varphi_{mn}^{\text{discrete}}(t)$ , where  $\varphi_{mn}^{\text{discrete}}(t)$  is the discretization of  $\varphi_{mn}^{\text{opt}}(t)$ . In this case,  $\Omega_{\text{RIS}}(t) = \Omega_{\text{RIS}}^{\text{opt}}(t) \times |\Upsilon(t)|^2 / (M^2 N^2)$  and the channel is characterized by Rician fading.

iii) *Constant*: The RIS controller applies constant reflection phase configuration with  $\varphi_{mn}(t) = \varphi_{mn}^{\text{const}}$ , where  $\varphi_{mn}^{\text{const}}$  is the optimal reflection phase at the initial instant, that is,  $\varphi_{mn}^{\text{const}} = \varphi_{mn}^{\text{opt}}(0)$ . In this case,  $\Omega_{\text{RIS}}(t) = \Omega_{\text{RIS}}^{\text{opt}}(t) |\Upsilon(t)|^2 / (M^2 N^2)$  and the channel is characterized by Rician fading.

iv) *Random*: The RIS controller applies random uniform reflection phase configuration with  $\varphi_{mn}(t) \sim \mathcal{U}[-\pi, \pi]$ . Then, the channel is characterized by Rayleigh fading with  $K^{\text{vir}}(t) = \Omega_{\text{RIS}}^{\text{opt}}(t) / (MN \sum_{\ell} P_{\ell}(t))$  being the power ratio between the RIS and NLoS components.

##### B. Performance Analysis

1) *Power Delivering Capability of RIS*: We first investigate the reflection phase of a  $200 \times 200$ -unit square RIS, that is, RIS<sub>B</sub>, under optimal reflection phase configuration in Fig. 4 based on (2). The phase values are normalized by modulo dividing  $2\pi$ . It shows that the phase-shift values show periodicity over the array at  $t = 0$ , which means that different RIS units share the same reflection phase in order to reflect the incident waves towards the target point. After

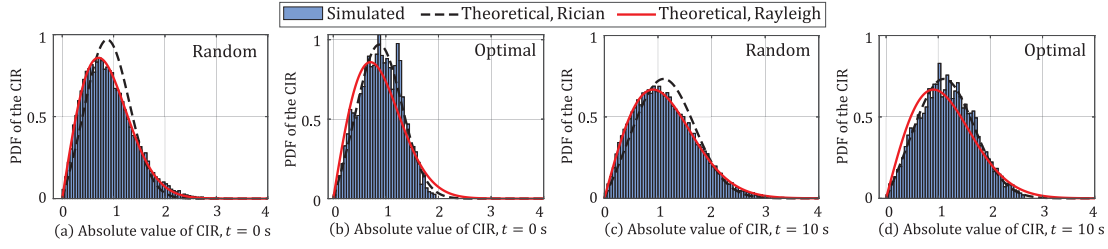


Fig. 6. Fading characteristics of the proposed RIS auxiliary channel model where  $K^{\text{vir}}(0) = 1.5$  and  $K^{\text{vir}}(10) = 1.31$ .

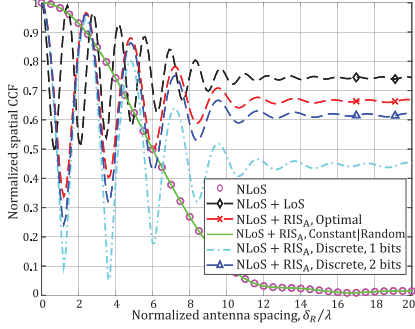


Fig. 7. Normalized spatial CCFs of different components with different RIS reflection phase configurations at  $t = 2$  s ( $v_T = 5$  m/s,  $\gamma_T = -\frac{\pi}{6}$ ,  $\eta_T = \frac{\pi}{24}$ ,  $v_R = 2$  m/s,  $\gamma_R = \frac{\pi}{6}$ ).

a time interval of  $t = 5$  s, the phase pattern changes, but the periodicity of phase values still holds. We observe that the reflection phase of the RIS units vary continuously with moving time of the UAV and MR. This is because we consider that the phase-shift profile of each RIS unit is a continuous function under optimal reflection phase configuration. This indicates the requirement of real-time RIS reflection phase control. Moreover, Fig. 4 implies that the theoretical optimal reflection phase of the central RIS unit changes slightly and much more slowly than that of the corner RIS unit. Thus, the RIS controller can choose to update the actual reflection phase of the central RIS unit less frequently than that of the corner RIS unit, which means more resources are saved and the cost of the system implementation is reduced.

In Fig. 5, we study the power delivering capability of RIS under optimal reflection phase configuration, which is characterized by  $\Omega_{\text{RIS}}^{\text{opt}}$  in (3). It shows the  $\Omega_{\text{RIS}}^{\text{opt}}$  firstly decreases and then increases as  $\xi_{\text{RIS}}^{\text{TR}}$  increases, where the inflexion occurs at  $\xi_{\text{RIS}}^{\text{TR}} = \xi_{\text{RIS}}^{\text{T}}/2$ . It also implies the  $\Omega_{\text{RIS}}^{\text{opt}}$  decreases as the  $\xi_{\text{RIS}}^{\text{TR}}$  or  $\beta_{\text{in}}$  increases. When the  $\xi_{\text{RIS}}^{\text{TR}}$  is relatively small, such as  $\xi_{\text{RIS}}^{\text{TR}} = 80$  or  $100$  m, the RIS has the ability to provide positive power gain ( $\Omega_{\text{RIS}}^{\text{opt}} > 1$ ) than LoS path at arbitrary location even with a relatively large incident angle  $\pi/3$  or  $\pi/6$ , respectively, motivating the use of RIS in *short-range scenarios*, i.e., indoor scenarios. Then, by comparing the curves with  $\xi_{\text{RIS}}^{\text{TR}} = 200$  m, we find that some locations of the RIS will achieve a power scaling factor larger than 1 when we increase the number of RIS units from 200 to 280. Overall, the results in Fig. 5 are consistent with the theoretical results in (3). They show how the power delivering capability of RIS will change with different system parameters settings, which provides guidelines for the practical RIS-assisted communication systems design. Specifically, it implies that a closer location of the RIS to the terminal (UAV or MR), a smaller normal

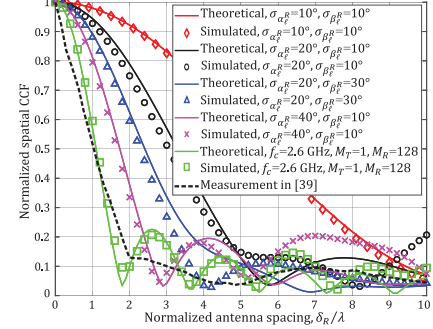


Fig. 8. Normalized spatial CCFs of the proposed channel model with different cluster angle spread at  $t = 2$  s ( $v_T = 5$  m/s,  $\gamma_T = -\frac{\pi}{6}$ ,  $\eta_T = \frac{\pi}{24}$ ,  $v_R = 2$  m/s,  $\gamma_R = \frac{\pi}{6}$ ).

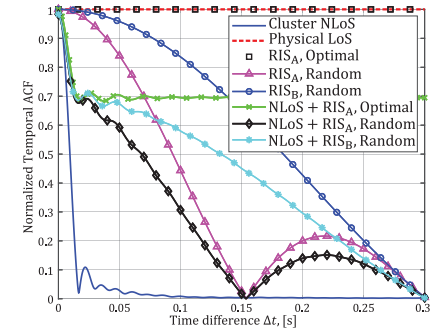


Fig. 9. Temporal ACFs of different components at  $t = 2$  s ( $v_T = 5$  m/s,  $\gamma_T = 0$ ,  $\eta_T = \pi/2$ ,  $v_R = 5$  m/s,  $\gamma_R = \pi$ ).

incident angle of the signals on RIS, or a larger number of RIS units will result in a higher power delivering capability of RIS, leading to more received power at the receiver.

2) *Fading Characterization*: By utilizing (5)-(6), we investigate the fading characteristics of the proposed channel model in Fig. 6 under optimal and random reflection phase configurations. By comparing the simulated results with theoretical ones, we observe that the proposed channel model tends to be characterized by Rician fading under optimal reflection phase configuration, whereas by Rayleigh fading under random uniform reflection phase configuration. The proposed channel model also satisfies Rician fading under discrete/constant reflection phase configuration but with different fading parameters as compared to optimal reflection phase configuration. Moreover, Fig. 6 reveals that the proposed channel model show different fading parameters at different time instants, which verifies the non-stationarity of the channel model.

3) *Time-Varying Spatial CCF*: In Fig. 7, we compare the spatial CCFs of different components under different RIS reflection phase configurations when the mobile terminals

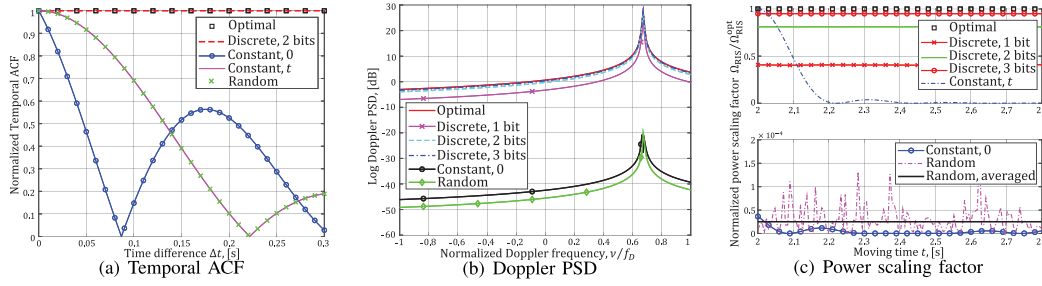


Fig. 10. Channel characteristics of the RIS component in different RIS reflection phase configurations,  $t = 2$  s.

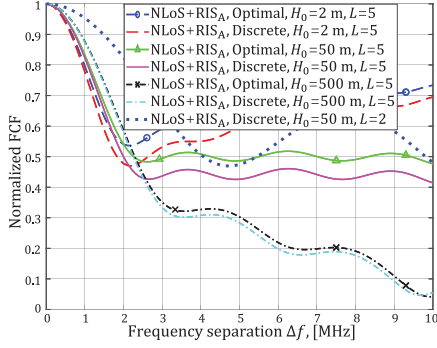


Fig. 11. Normalized FCFs of the proposed channel model with different UAV height and cluster number.

adopt a general mobility model based on (26)-(27). It shows that the channel with optimal/discrete reflection phase configuration shows similar decreasing trend of the spatial CCFs as compared to that with LoS path, which means that the RIS component behaves similarly to the physical LoS path. The spatial CCFs of the channel with constant/random reflection phase configuration coincides with those of the NLoS component owing to the very small power gains. In summary, constant/random reflection phase configuration results in smaller spatial CCFs and hence are more benefit for channel spatial diversity than discrete/optimal reflection phase configuration. On the other hand, they cause much smaller power gains of the RIS path, and hence less power is delivered to the MR, leading to insignificant performance improvement as compared to the channel without RIS. Furthermore, we observe that the results curves firstly fluctuate and then gradually stabilize as the antenna spacing increases. The spatial CCF of the RIS component, that is,  $\rho_{(p,q),(p',q')}^{\text{RIS}}(t, \Delta p, \Delta q)$  in (26), is a complex exponential function of antenna spacing with constant absolute value, whereas the spatial CCF of the NLoS component, that is,  $\rho_{(p,q),(p',q'),\ell}^{\text{NLoS}}(t, \Delta p, \Delta q)$  in (27), is also a complex exponential function of antenna spacing but with decreasing absolute value. As a consequence, the linearly superimposed results curves are also complex exponential functions of antenna spacing. They firstly fluctuate and then gradually stabilize at a fixed value, that is,  $\frac{K^{\text{vir}}(t)}{K^{\text{vir}}(t)+1}$ , as the antenna spacing increases. By improving the accuracy of the configuration of RIS reflection phase, we can stabilize the performance of the spatial CCFs.

Then, in Fig. 8 we investigate the impact of cluster angle spread on channel spatial CCFs by setting the RIS component as zero based on (27). These representative parameter settings are enough to reveal the fact that by increasing the cluster

angle spread, the channel spatial CCF decreases, and hence the channel is more likely to benefit from spatial diversity. This agrees with the results in [21]. Overall, the channel shows different propagation characteristics under different model parameter values settings, resulting in different overall performance of the communication systems. Moreover, it shows that the simulated results agree with the theoretical ones, which verify the correctness of the derived spatial CCF of the proposed channel model. In addition, by setting the simulation parameters according to the measurement setup in [39], Fig. 8 indicates that the curves of theoretical/simulated results of the proposed channel model, they are, the curves with  $f_c = 2.6$  GHz (also the curves in green), are in agreement with those of measurement results in [39]. This verifies the accuracy of the proposed channel model.

4) *Time-Varying Temporal ACF and Doppler PSD*: In Fig. 9, we take a comparison of the channel temporal correlations of different components of the proposed channel model based on (30)-(31), where the results show RIS<sub>A</sub> provides faster decline on temporal ACF than RIS<sub>B</sub> due to larger spatial spread. It also shows that the RIS component provides the same temporal ACF as the physical LoS path under optimal reflection phase configuration. When random uniform reflection phase configuration is adopted, on the contrary, the RIS component provides a cluster NLoS-shaped decline on temporal ACF but with a much slower decreasing trend. Moreover, Fig. 9 reveals that the existence of RIS will slow down the decline of the temporal correlation of the LoS-obstructed channel, resulting in longer channel coherence time and less frequently channel estimation. Then, in Fig. 10 we study the impact of RIS reflection phase configurations on temporal ACFs, Doppler PSDs, and RIS power delivering capabilities based on (30), (33), and (1), respectively, where “Constant,  $t$ ” implies  $\varphi_{mn}^{\text{const}} = \varphi_{mn}^{\text{opt}}(t = 2)$ . Figs. 10(a)-(b) reveal that the constant and random uniform reflection phase configurations behave similarly in both temporal ACFs and Doppler PSDs, whereas the discrete and optimal reflection phase configurations behave similarly in both temporal ACFs and Doppler PSDs, which highlights the advantage of discrete reflection phase configuration. Meanwhile, Fig. 10(c) indicates that the discrete reflection phase configuration has the ability to provide a near-optimal performance with several controlling bits (generally two bits is acceptable) and significant reduction in the implementation complexity, which motivates the usage of *discrete* RIS reflection phase configuration.



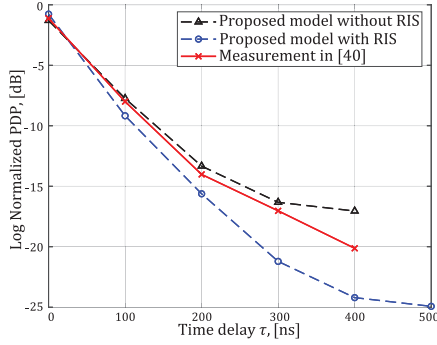


Fig. 12. Normalized PDPs of the proposed channel model.

5) *Time-Varying FCF and PDP*: In Fig. 11 we investigate the impact of UAV's height on channel frequency propagation characteristics based on (37), where the results indicate that the channel FCF decreases slower when increasing the UAV's height, resulting in larger coherence bandwidth and higher throughput. Also, it implies that a 2-bit discrete reflection phase configuration can approach the optimal reflection phase configuration well, which is consistent with the results in Fig. 10. Moreover, Fig. 11 indicates the channel with less cluster shows higher frequency correlation and hence larger coherence bandwidth, which agrees with the results in [21]. By using (38), we simulate the PDP of the proposed channel model under optimal reflection phase configuration in Fig. 12. The results show that the power is more centered in the first path when the RIS exists, which is similar to the results in [22] with LoS path exists. By setting the RIS component as zero, Fig. 12 shows the PDPs of the proposed channel model without RIS agree with the measurements in [40] well, which validates the effectiveness of the proposed channel model.

## V. CONCLUSION

In this paper, we have developed a 3D non-stationary MIMO wideband end-to-end channel model for RIS auxiliary UAV-to-ground mmWave communications, which has the ability to capture the non-stationarity of UAV channels and the sparsity of mmWave channels. The proposed modeling solution can accurately describe the physical properties of RIS auxiliary communication channels by modeling the RIS as a virtual cluster and by developing end-to-end CIRs to characterize the physical properties of the underlying propagation channels. The impact of RIS reflection phase configurations on channel statistical properties has been investigated, where the results show that the RIS component behaves like physical LoS path under optimal/discrete reflection phase configuration and a 2-bit discrete reflection phase configuration can approach the performance of optimal reflection phase configuration but with significant reduction in realization complexity. Moreover, the results demonstrate that a smaller incident angle and a closer location of RIS to the transceivers can result in higher received power; meanwhile, the fading of the RIS auxiliary channel is generally characterized by Rician fading, whereas by Rayleigh fading when random uniform reflection phase configuration is adopted under Central Limit Theorem. Finally, the agreement between the theoretical and simulated as well as measurement results validates the effectiveness of the proposed

channel model, which can inform the design of practical RIS-assisted communication systems and help researchers as well as industry communities for system performance analysis and algorithm validations via simulations.

As future work, we point out four potential directions: i) statistical characterization of the RIS auxiliary communication channels in short-range near-field scenarios; ii) investigate the new propagation characteristics in multiple RISs cooperative communications; iii) conduct measurements to further validate the proposed channel model; iv) perform comparisons in terms of efficiency and/or complexity between the proposed channel model and the existing ones.

## APPENDIX A

We define  $P_t$  as the transmitting power and  $G_t$  as the beam-forming gain of the UAV antenna array. Then, the received power of the  $(m, n)$ -th RIS unit can be calculated by

$$P_{mn}^{\text{in}}(t) = \frac{P_t G_t}{4\pi \xi_{mn}^{T^2}(t)} \times d_M d_N \cos \beta_{\text{in}}(t), \quad (39)$$

where  $\xi_{mn}^T(t) = \xi_{\text{RIS}}^T(t) - k_m d_M \sin \beta_{\text{in}}(t) \cos \alpha_{\text{in}}(t) - k_n d_N \sin \beta_{\text{in}}(t) \sin \alpha_{\text{in}}(t)$  denotes the distance from the center of UAV antenna array to the  $(m, n)$ -th RIS unit. Then, the reflected power by the  $(m, n)$ -th RIS unit can be expressed as [41]

$$P_{mn}^{\text{out}}(t) = \frac{P_t G_t \times d_M d_N \cos \beta_{\text{in}}(t)}{4\pi \xi_{mn}^{T^2}(t)} |\chi_{mn}(t) e^{j\varphi_{mn}(t)}|^2. \quad (40)$$

Let  $G_r$  be the combining gain of the MR antenna array, thus the effective aperture of the receiving antenna can be expressed as  $S_{r,ap} = G_r \lambda^2 / 4\pi$ . Then, the received power of the MR from the  $(m, n)$ -th RIS unit can be calculated by

$$P_{mn}^r(t) = \frac{P_{mn}^{\text{out}}(t)}{4\pi \xi_{mn}^{R^2}(t)} S_{r,ap}, \quad (41)$$

where  $\xi_{mn}^R(t) = \xi_{\text{RIS}}^R(t) - k_m d_M \sin \beta_{\text{out}}(t) \cos \alpha_{\text{out}}(t) - k_n d_N \sin \beta_{\text{out}}(t) \sin \alpha_{\text{out}}(t)$  denotes the distance from the center of MR antenna array to the  $(m, n)$ -th RIS unit. By substituting (40) into (41), we can obtain

$$P_{mn}^r(t) = \frac{P_t G_t G_r \lambda^2 d_M d_N \cos \beta_{\text{in}}(t)}{(4\pi)^3 \xi_{mn}^{T^2}(t) \xi_{mn}^{R^2}(t)} |\chi_{mn}(t) e^{j\varphi_{mn}(t)}|^2. \quad (42)$$

As indicated in [42], the received power  $P_{mn}^r(t)$  can also be expressed as

$$P_{mn}^r(t) = \frac{|E_{mn}^r(t)|^2}{2\eta} S_{r,ap}, \quad (43)$$

where  $\eta$  is the intrinsic impedance ( $\simeq 120\pi$  ohms for free-space), and  $E_{mn}^r(t)$  is the received radiation electric field. By combining (42) and (43),  $E_{mn}^r(t)$  can be solved as

$$\begin{aligned} E_{mn}^r(t) &= \sqrt{\frac{2\eta P_t G_t G_r \lambda^2 d_M d_N \cos \beta_{\text{in}}(t)}{(4\pi)^3 S_{r,ap}}} \times \frac{\chi_{mn}(t) e^{j\varphi_{mn}(t)}}{\xi_{mn}^T(t) \xi_{mn}^R(t)} \\ &\times e^{j\frac{2\pi}{\lambda} v_T t \left( \cos(\alpha_{\text{RIS}}^T(t) - \gamma_T) \cos \beta_{\text{RIS}}^T(t) \cos \eta_T + \sin \beta_{\text{RIS}}^T(t) \sin \eta_T \right)} \\ &\times e^{j\frac{2\pi}{\lambda} v_R t \cos(\alpha_{\text{RIS}}^R(t) - \gamma_R) \cos \beta_{\text{RIS}}^R(t)} e^{-j\frac{2\pi}{\lambda} (\xi_{mn}^T(t) + \xi_{mn}^R(t))}. \end{aligned} \quad (44)$$

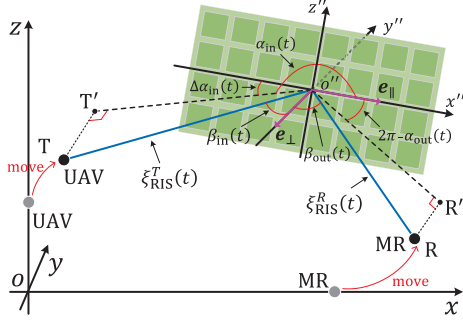


Fig. 13. Illustration of incident and reflected angles on RIS. T and R denote the positions of UAV and MR, respectively, whereas T' and R' are their projections on the  $x''-o''-z''$  plane, respectively. The  $x''-y''-z''$  is established over the RIS and can be derived by rotating  $x'-y'-z'$  in Fig. 2(b) by a horizontal rotation angle of  $\theta_I$  and a vertical rotation angle of  $\epsilon_I$ , respectively.

The superimposed received electric field can be calculated by  $E_r(t) = \sum_{m=1}^M \sum_{n=1}^N E_{mn}^r(t)$ . Similar to (43), the MR received reflection power from RIS can be expressed as

$$\begin{aligned} P_r(t) &= \frac{|E_r(t)|^2}{2\eta} S_{r,ap} \\ &= P_r^{free}(t) \times \frac{d_M d_N \cos \beta_{in}(t) (\xi_{RIS}^T(t) + \xi_{RIS}^R(t))^2}{4\pi} \\ &\quad \times \left| \sum_{m=1}^M \sum_{n=1}^N \frac{\chi_{mn}(t) e^{j(\varphi_{mn}(t) - \varphi_{mn}^{dis}(t))}}{\xi_{mn}^T(t) \xi_{mn}^R(t)} \right|^2, \end{aligned} \quad (45)$$

where  $P_r^{free}(t) = \frac{P_t G_t G_r \lambda^2}{(4\pi)^2 (\xi_{RIS}^T(t) + \xi_{RIS}^R(t))^2}$  is the received power of the same-distance free path and  $\varphi_{mn}^{dis}(t)$  is the distance-related phase term which is related with index  $m$  and  $n$ , that is,

$$\begin{aligned} \varphi_{mn}^{dis}(t) &= \frac{-2\pi k_m d_M}{\lambda} (\sin \beta_{in}(t) \cos \alpha_{in}(t) + \sin \beta_{out}(t) \cos \alpha_{out}(t)) \\ &\quad - \frac{2\pi k_n d_N}{\lambda} (\sin \beta_{in}(t) \sin \alpha_{in}(t) + \sin \beta_{out}(t) \sin \alpha_{out}(t)), \end{aligned} \quad (46)$$

where  $k_m = \frac{2m-M-1}{2}$  and  $k_n = \frac{2n-N-1}{2}$ . Therefore, Theorem 1 holds.

#### APPENDIX B

In Fig. 13, we illustrate the time-varying incident and reflected angles on RIS, which are defined based on the local coordinate system  $x''-y''-z''$ . Then, the unit vector along the positive direction of  $x''$ -axis and that along the negative direction of  $y''$ -axis can be expressed as  $\mathbf{e}_{\parallel} = [\cos \theta_I, \sin \theta_I, 0]^T$  and  $\mathbf{e}_{\perp} = [\sin \theta_I \cos \epsilon_I, -\cos \theta_I \cos \epsilon_I, -\sin \epsilon_I]^T$ , respectively. At time  $t$ , the positions of UAV and MR are at points  $\mathbf{T} = (v_T t \cos \eta_T \cos \gamma_T, v_T t \cos \eta_T \sin \gamma_T, H_0 + v_T t \sin \eta_T)$  and  $\mathbf{R} = (\xi_R + v_R t \cos \gamma_R, v_R t \sin \gamma_R, 0)$ , respectively. Therefore, the distance vectors from the center of RIS to UAV and to MR, denoted by  $\mathbf{d}_{o''}^T(t)$  and  $\mathbf{d}_{o''}^R(t)$ , respectively, can be

expressed as

$$\mathbf{d}_{o''}^T(t) = \mathbf{T} - \mathbf{o}'' = \begin{bmatrix} v_T t \cos \eta_T \cos \gamma_T - x_I \\ v_T t \cos \eta_T \sin \gamma_T - y_I \\ H_0 + v_T t \sin \eta_T - z_I \end{bmatrix}, \quad (47)$$

$$\mathbf{d}_{o''}^R(t) = \mathbf{R} - \mathbf{o}'' = \begin{bmatrix} \xi_R + v_R t \cos \gamma_R - x_I \\ v_R t \sin \gamma_R - y_I \\ -z_I \end{bmatrix}, \quad (48)$$

where  $\|\mathbf{d}_{o''}^T(t)\| = \xi_{RIS}^T(t)$  and  $\|\mathbf{d}_{o''}^R(t)\| = \xi_{RIS}^R(t)$ . Next, we can derive the normal incident angle from UAV to RIS and normal reflected angle from RIS to MR as (49) and (50), respectively, as shown at the top of next page. Once the normal incident  $\beta_{in}(t)$  and reflected  $\beta_{out}(t)$  angles are obtained, the distance vectors from  $\mathbf{o}''$  to projection points T' and R', denoted by  $\mathbf{d}_{o''}^{T'}(t)$  and  $\mathbf{d}_{o''}^{R'}(t)$ , respectively, can be derived by

$$\begin{aligned} \mathbf{d}_{o''}^{T'}(t) &= \mathbf{d}_{o''}^T(t) - \xi_{RIS}^T(t) \cos \beta_{in}(t) \cdot \mathbf{e}_{\perp} \\ &= \begin{bmatrix} r_T^x(t) - x_I - \xi_{RIS}^T(t) \cos \beta_{in}(t) \sin \theta_I \cos \epsilon_I \\ r_T^y(t) - y_I + \xi_{RIS}^T(t) \cos \beta_{in}(t) \cos \theta_I \cos \epsilon_I \\ H_0 + r_T^z(t) - z_I + \xi_{RIS}^T(t) \cos \beta_{in}(t) \sin \epsilon_I \end{bmatrix}, \quad (51) \\ \mathbf{d}_{o''}^{R'}(t) &= \mathbf{d}_{o''}^R(t) - \xi_{RIS}^R(t) \cos \beta_{out}(t) \cdot \mathbf{e}_{\perp} \\ &= \begin{bmatrix} \xi_R + r_R^x(t) - x_I - \xi_{RIS}^R(t) \cos \beta_{out}(t) \sin \theta_I \cos \epsilon_I \\ r_R^y(t) - y_I + \xi_{RIS}^R(t) \cos \beta_{out}(t) \cos \theta_I \cos \epsilon_I \\ r_R^z(t) - z_I + \xi_{RIS}^R(t) \cos \beta_{out}(t) \sin \epsilon_I \end{bmatrix}. \end{aligned} \quad (52)$$

Therefore, the azimuth incident angle from UAV to RIS, that is,  $\alpha_{in}(t)$ , and the azimuth reflected angle from RIS to MR, that is,  $\alpha_{out}(t)$ , can be respectively expressed as (53) and (54), where  $\Delta \alpha_{in}(t)$  in (53) is expressed as (55), both are shown at the top of next page.

#### APPENDIX C

Let us take the propagation between the  $(p \rightarrow q)$ -th transmit-receive antenna pair as an example. We assume that an unmodulated carrier is transmitted, i.e.,  $s(t) = 1$ , then the received complex envelope without noise can be obtained by convolving the transmitted signal  $s(t)$  with the channel response  $h_{pq}(t, \tau, \boldsymbol{\Theta}_T, \boldsymbol{\Theta}_R)$  as [32]

$$\begin{aligned} r(t) &= \int_{-\infty}^{\infty} h_{pq}(t, \tau, \boldsymbol{\Theta}_T, \boldsymbol{\Theta}_R) s(t - \tau) d\tau \\ &= h_{pq}^{\text{RIS}}(t) + \sum_{\ell=1}^L h_{\ell, pq}(t). \end{aligned} \quad (56)$$

With the phases  $\varphi_{\ell, i}$  in (6) being independent and identically distributed random variables as well as the Central Limit Theorem,  $h_{\ell, pq}(t)$  approaches a Rayleigh process with zero mean and variance of  $P_{\ell}(t)$  when  $I$  is large enough [22]. Moreover, with the uncorrelated scattering assumption [32],  $g(t) = \sum_{\ell=1}^L h_{\ell, pq}(t)$  is the summation of  $L$  independent Rayleigh

$$\beta_{\text{in}}(t) = \arccos \frac{\mathbf{e}_{\perp}^T \cdot \mathbf{d}_{o''}^T(t)}{\|\mathbf{e}_{\perp}\| \cdot \|\mathbf{d}_{o''}^T(t)\|} = \arccos \frac{[(r_T^x(t) - x_I) \sin \theta_I - (r_T^y(t) - y_I) \cos \theta_I] \cos \epsilon_I - (H_0 + r_T^z(t) - z_I) \sin \epsilon_I}{\xi_{\text{RIS}}^T(t)}, \quad (49)$$

$$\beta_{\text{out}}(t) = \arccos \frac{\mathbf{e}_{\perp}^T \cdot \mathbf{d}_{o''}^R(t)}{\|\mathbf{e}_{\perp}\| \cdot \|\mathbf{d}_{o''}^R(t)\|} = \arccos \frac{(\xi_R + r_R^x(t) - x_I) \sin \theta_I \cos \epsilon_I - (r_R^y(t) - y_I) \cos \theta_I \cos \epsilon_I + z_I \sin \epsilon_I}{\xi_{\text{RIS}}^R(t)}. \quad (50)$$

$$\alpha_{\text{in}}(t) = \begin{cases} \pi - \Delta\alpha_{\text{in}}(t), & \text{if } H_0 + v_T t \sin \eta_T - z_I + \xi_{\text{RIS}}^T(t) \cos \beta_{\text{in}}(t) \sin \epsilon_I > 0 \\ \pi + \Delta\alpha_{\text{in}}(t), & \text{if } H_0 + v_T t \sin \eta_T - z_I + \xi_{\text{RIS}}^T(t) \cos \beta_{\text{in}}(t) \sin \epsilon_I \leq 0, \end{cases} \quad (53)$$

$$\alpha_{\text{out}}(t) = 2\pi - \arccos \frac{\mathbf{e}_{\parallel}^T \cdot \mathbf{d}_{o''}^R(t)}{\|\mathbf{e}_{\parallel}\| \cdot \|\mathbf{d}_{o''}^R(t)\|} = 2\pi - \arccos \frac{(\xi_R + v_R t \cos \gamma_R - x_I) \cos \theta_I + (v_R t \sin \gamma_R - y_I) \sin \theta_I}{\|\mathbf{d}_{o''}^R(t)\|}, \quad (54)$$

$$\Delta\alpha_{\text{in}}(t) = \arccos \frac{(-\mathbf{e}_{\parallel})^T \cdot \mathbf{d}_{o''}^T(t)}{\|(-\mathbf{e}_{\parallel})\| \cdot \|\mathbf{d}_{o''}^T(t)\|} = \arccos \frac{(x_I - v_T t \cos \eta_T \cos \gamma_T) \cos \theta_I + (y_I - v_T t \cos \eta_T \sin \gamma_T) \sin \theta_I}{\|\mathbf{d}_{o''}^T(t)\|}. \quad (55)$$

processes with zero mean and variance of  $\sum_{\ell=1}^L P_{\ell}(t)$ , that is,  $\mathbb{E}\{g(t)\} = 0$  and  $\text{Var}\{g(t)\} = \sum_{\ell=1}^L P_{\ell}(t)$ .

The RIS component  $h_{pq}^{\text{RIS}}(t) = \text{Re}\{h_{pq}^{\text{RIS}}(t)\} + j \cdot \text{Im}\{h_{pq}^{\text{RIS}}(t)\}$  is a deterministic process, then we can rewrite (56) as

$$j \cdot \text{Im}\{r(t)\} + \text{Re}\{r(t)\} = j \cdot (\text{Im}\{h_{pq}^{\text{RIS}}(t)\} + \text{Im}\{g(t)\}) + \text{Re}\{h_{pq}^{\text{RIS}}(t)\} + \text{Re}\{g(t)\}. \quad (57)$$

Accordingly, we can observe that the real part  $\text{Re}\{r(t)\}$  and imaginary part  $\text{Im}\{r(t)\}$  are Gaussian random processes with different mean values  $\text{Re}\{h_{pq}^{\text{RIS}}(t)\}$  and  $\text{Im}\{h_{pq}^{\text{RIS}}(t)\}$ , respectively, but the same variance  $\frac{1}{2} \sum_{\ell=1}^L P_{\ell}(t)$ . Moreover, the correlation function between  $\text{Re}\{r(t)\}$  and  $\text{Im}\{r(t)\}$  can be expressed as

$$\begin{aligned} \text{Cov}(\text{Re}\{r(t)\}, \text{Im}\{r(t)\}) &= \mathbb{E}\{(\text{Re}\{r(t)\} - \text{Re}\{h_{pq}^{\text{RIS}}(t)\})^* \\ &\quad \times (\text{Im}\{r(t)\} - \text{Im}\{h_{pq}^{\text{RIS}}(t)\})\} \\ &= 0. \end{aligned} \quad (58)$$

Therefore,  $\text{Re}\{r(t)\}$  and  $\text{Im}\{r(t)\}$  are two independent Gaussian random processes with non-zero means and same variance. Thus,  $r(t)$  is a Rice process and the fading of the proposed channel model is characterized by Rician fading with the non-centrality parameter  $[\text{Re}\{h_{pq}^{\text{RIS}}(t)\}]^2 + [\text{Im}\{h_{pq}^{\text{RIS}}(t)\}]^2 = |h_{pq}^{\text{RIS}}(t)|^2 = \Omega_{\text{RIS}}(t)$ . Thus, Corollary 2 holds.

## REFERENCES

- [1] W. Saad, M. Bennis, and M. Chen, "A vision of 6G wireless systems: Applications, trends, technologies, and open research problems," *IEEE Neww.*, vol. 34, no. 3, pp. 134–142, May/Jun. 2020.
- [2] M. Mozaffari, W. Saad, M. Bennis, Y.-H. Nam, and M. Debbah, "A tutorial on UAVs for wireless networks: Applications, challenges, and open problems," *IEEE Commun. Surveys Tuts.*, vol. 21, no. 3, pp. 2334–2360, 3rd Quart., 2019.
- [3] Z. Xiao, P. Xia, and X.-G. Xia, "Enabling UAV cellular with millimeter-wave communication: Potentials and approaches," *IEEE Commun. Mag.*, vol. 54, no. 5, pp. 66–73, May 2016.
- [4] E. Basar, M. Di Renzo, J. De Rosny, M. Debbah, M. Alouini, and R. Zhang, "Wireless communications through reconfigurable intelligent surfaces," *IEEE Access*, vol. 7, pp. 116753–116773, 2019.
- [5] S. Li, B. Duo, X. Yuan, Y.-C. Liang, and M. Di Renzo, "Reconfigurable intelligent surface assisted UAV communication: Joint trajectory design and passive beamforming," *IEEE Wireless Commun. Lett.*, vol. 9, no. 5, pp. 716–720, May 2020.
- [6] H. Lu, Y. Zeng, S. Jin, and R. Zhang, "Enabling panoramic full-angle reflection via aerial intelligent reflecting surface," in *Proc. IEEE ICC*, Dublin, Ireland, Jun. 2020, pp. 1–6.
- [7] C. Pradhan, A. Li, L. Song, B. Vucetic, and Y. Li, "Hybrid precoding design for reconfigurable intelligent surface aided mmWave communication systems," *IEEE Wireless Commun. Lett.*, vol. 9, no. 7, pp. 1041–1045, Jul. 2020.
- [8] N. S. Perovic, M. Di Renzo, and M. F. Flanagan, "Channel capacity optimization using reconfigurable intelligent surfaces in indoor mmWave environments," in *Proc. IEEE ICC*, Dublin, Ireland, Jun. 2020, pp. 1–6.
- [9] W. Tang *et al.*, "Wireless communications with programmable metasurface: New paradigms, opportunities, and challenges on transceiver design," *IEEE Wireless Commun.*, vol. 27, no. 2, pp. 180–187, Apr. 2020.
- [10] T. Hou, Y. Liu, Z. Song, X. Sun, Y. Chen, and L. Hanzo, "Reconfigurable intelligent surface aided NOMA networks," *IEEE J. Sel. Areas Commun.*, vol. 38, no. 11, pp. 2575–2588, Nov. 2020.
- [11] E. Basar, "Reconfigurable intelligent surface-based index modulation: A new beyond MIMO paradigm for 6G," *IEEE Trans. Commun.*, vol. 68, no. 5, pp. 3187–3196, May 2020.
- [12] J. He, H. Wymeersch, T. Sanguanpuak, O. Silven, and M. Juntti, "Adaptive beamforming design for mmWave RIS-aided joint localization and communication," in *Proc. IEEE WCNC Workshops*, Seoul, South Korea, Apr. 2020, pp. 1–6.
- [13] O. Özdogan, E. Björnson, and E. G. Larsson, "Intelligent reflecting surfaces: Physics, propagation, and pathloss modeling," *IEEE Wireless Commun. Lett.*, vol. 9, no. 5, pp. 581–585, May 2020.
- [14] F. H. Danufane, M. D. Renzo, J. de Rosny, and S. Tretyakov, "On the path-loss of reconfigurable intelligent surfaces: An approach based on Green's theorem applied to vector fields," *IEEE Trans. Commun.*, vol. 69, no. 8, pp. 5573–5592, Aug. 2021.
- [15] J. C. B. Garcia, A. Sibille, and M. Kamoun, "Reconfigurable intelligent surfaces: Bridging the gap between scattering and reflection," *IEEE J. Sel. Areas Commun.*, vol. 38, no. 11, pp. 2538–2547, Nov. 2020.
- [16] W. Tang *et al.*, "Wireless communications with reconfigurable intelligent surface: Path loss modeling and experimental measurement," *IEEE Trans. Wireless Commun.*, vol. 20, no. 1, pp. 421–439, Jan. 2021.
- [17] M. Najafi, V. Jamali, R. Schober, and H. V. Poor, "Physics-based modeling and scalable optimization of large intelligent reflecting surfaces," *IEEE Trans. Commun.*, vol. 69, no. 4, pp. 2673–2691, Apr. 2021.
- [18] H. Jiang *et al.*, "A general wideband non-stationary stochastic channel model for intelligent reflecting surface-assisted MIMO communications," *IEEE Trans. Wireless Commun.*, vol. 20, no. 8, pp. 5314–5328, Aug. 2021.
- [19] E. Basar and I. Yildirim, "Reconfigurable intelligent surfaces for future wireless networks: A channel modeling perspective," *IEEE Wireless Commun.*, vol. 28, no. 3, pp. 108–114, Jun. 2021.
- [20] R. He, B. Ai, G. Wang, M. Yang, C. Huang, and Z. Zhong, "Wireless channel sparsity: Measurement, analysis, and exploitation in estimation," *IEEE Wireless Commun.*, vol. 28, no. 4, pp. 113–119, Aug. 2021.
- [21] R. He, B. Ai, G. L. Stüber, G. Wang, and Z. Zhong, "Geometrical-based modeling for millimeter-wave MIMO mobile-to-mobile channels," *IEEE Trans. Veh. Technol.*, vol. 67, no. 4, pp. 2848–2863, Apr. 2018.



- [22] B. Xiong, Z. Zhang, J. Zhang, H. Jiang, J. Dang, and L. Wu, "Novel multi-mobility V2X channel model in the presence of randomly moving clusters," *IEEE Trans. Wireless Commun.*, vol. 20, no. 5, pp. 3180–3195, May 2021.
- [23] *Study on Channel Model for Frequencies From 0.5 to 100 GHz*, document 3GPP TR 38.901, Version 16.1.0, Release 16, Dec. 2019.
- [24] H. Jiang, Z. Zhang, L. Wu, J. Dang, and G. Gui, "A 3-D non-stationary wideband geometry-based channel model for MIMO vehicle-to-vehicle communications in tunnel environments," *IEEE Trans. Veh. Technol.*, vol. 68, no. 7, pp. 6257–6271, Jul. 2019.
- [25] M. K. Samimi and T. S. Rappaport, "3-D millimeter-wave statistical channel model for 5G wireless system design," *IEEE Trans. Microw. Theory Techn.*, vol. 64, no. 7, pp. 2207–2225, Jul. 2016.
- [26] H. Jiang, Z. Zhang, J. Dang, and L. Wu, "Analysis of geometric multibounced virtual scattering channel model for dense urban street environments," *IEEE Trans. Veh. Technol.*, vol. 66, no. 3, pp. 1903–1912, Mar. 2017.
- [27] M. A. Elmassallamy *et al.*, "Reconfigurable intelligent surfaces for wireless communications: Principles, challenges, and opportunities," *IEEE Trans. Cogn. Commun. Netw.*, vol. 6, no. 3, pp. 990–1002, Sep. 2020.
- [28] B. Matthiesen, E. Bjornson, E. De Carvalho, and P. Popovski, "Intelligent reflecting surface operation under predictable receiver mobility: A continuous time propagation model," *IEEE Wireless Commun. Lett.*, vol. 10, no. 2, pp. 216–220, Feb. 2021.
- [29] N. Yu *et al.*, "Light propagation with phase discontinuities: Generalized laws of reflection and refraction," *Science*, vol. 334, no. 6054, pp. 333–337, Oct. 2011.
- [30] Q. Wu and R. Zhang, "Intelligent reflecting surface enhanced wireless network: Joint active and passive beamforming design," in *Proc. IEEE GLOBECOM*, Abu Dhabi, United Arab Emirates, Dec. 2018, pp. 1–6.
- [31] J. Bian *et al.*, "A WINNER+ based 3-D non-stationary wideband MIMO channel model," *IEEE Trans. Wireless Commun.*, vol. 17, no. 3, pp. 1755–1767, Mar. 2018.
- [32] A. Goldsmith, *Wireless Communications*. Cambridge, U.K.: Cambridge Univ. Press, 2005.
- [33] Z. Ma, B. Ai, R. He, G. Wang, Y. Niu, and Z. Zhong, "A wideband non-stationary air-to-air channel model for UAV communications," *IEEE Trans. Veh. Technol.*, vol. 69, no. 2, pp. 1214–1226, Feb. 2020.
- [34] Z. Ma *et al.*, "Impact of UAV rotation on MIMO channel characterization for air-to-ground communication systems," *IEEE Trans. Veh. Technol.*, vol. 69, no. 11, pp. 12418–12431, Nov. 2020.
- [35] J. Li *et al.*, "On 3D cluster-based channel modeling for large-scale array communications," *IEEE Trans. Wireless Commun.*, vol. 18, no. 10, pp. 4902–4914, Oct. 2019.
- [36] S. Wu, C.-X. Wang, E.-H. M. Aggoune, M. M. Alwakeel, and X. You, "A general 3-D non-stationary 5G wireless channel model," *IEEE Trans. Commun.*, vol. 66, no. 7, pp. 3065–3078, Jul. 2018.
- [37] *Study on Enhanced LTE Support for Aerial Vehicles*, document 3GPP TR 36.777, Version 15.0.0, Release 15, Dec. 2017.
- [38] Y. Liu, C.-X. Wang, C. F. Lopez, G. Goussetis, Y. Yang, and G. K. Karagiannidis, "3D non-stationary wideband tunnel channel models for 5G high-speed train wireless communications," *IEEE Trans. Intell. Transp. Syst.*, vol. 21, no. 1, pp. 259–272, Jan. 2020.
- [39] S. Payami and F. Tufvesson, "Channel measurements and analysis for very large array systems at 2.6 GHz," in *Proc. EUCAP*, Prague, Czech Republic, Mar. 2012, pp. 433–437.
- [40] M. K. Samimi and T. S. Rappaport, "3-D statistical channel model for millimeter-wave outdoor mobile broadband communications," in *Proc. IEEE ICC*, London, U.K., Jun. 2015, pp. 2430–2436.
- [41] C. A. Balanis, *Antenna Theory: Analysis and Design*. Hoboken, NJ, USA: Wiley, 2016.
- [42] W. L. Stutzman and G. A. Thiele, *Antenna Theory and Design*. Hoboken, NJ, USA: Wiley, 2013.



**Baiping Xiong** received the B.Eng. degree in information engineering from Southeast University, Nanjing, China, in 2019, where he is currently pursuing the Ph.D. degree with the National Mobile Communications Research Laboratory.



**Zaichen Zhang** (Senior Member, IEEE) was born in Nanjing, China, in 1975. He received the B.S. and M.S. degrees in electrical and information engineering from Southeast University, Nanjing, in 1996 and 1999, respectively, and the Ph.D. degree in electrical and electronic engineering from The University of Hong Kong, Hong Kong, in 2002. From 2002 to 2004, he was a Post-Doctoral Fellow with the National Mobile Communications Research Laboratory, Southeast University. He joined the School of Information Science and Engineering, Southeast University, in 2004, where he is currently a Professor. He has published more than 200 articles and issued 50 patents. His current research interests include 6G mobile communication systems, optical wireless communications, and quantum information processing.



wireless communication networks, signal processing, machine learning, and AI-driven technologies.



**Hao Jiang** (Member, IEEE) received the B.S. and M.S. degrees in electrical and information engineering from the Nanjing University of Information Science and Technology, Nanjing, China, in 2012 and 2015, respectively, and the Ph.D. degree from Southeast University, Nanjing, in 2019. From 2017 to 2018, he was a Visiting Student with the Department of Electrical Engineering, Columbia University, New York, NY, USA. His current research interests include the general area of wireless channel measurements and modeling, B5G networks, signal processing, machine learning, and AI-driven technologies.

**Jiangfan Zhang** (Member, IEEE) received the B.Eng. degree in communication engineering from the Huazhong University of Science and Technology, Wuhan, China, in 2008, the M.Eng. degree in information and communication engineering from Zhejiang University, Hangzhou, China, 2011, and the Ph.D. degree in electrical engineering from Lehigh University, Bethlehem, PA, USA, in 2016. From 2016 to 2018, he was a Post-Doctoral Research Scientist with the Department of Electrical Engineering, Columbia University, New York, NY, USA.

Since 2018, he has been with the Department of Electrical and Computer Engineering, Missouri University of Science and Technology, Rolla, MO, USA, where he is currently an Assistant Professor. His research interests include signal processing, machine learning, and their applications to cybersecurity, cyber-physical systems, the Internet of Things, smart grids, and sonar processing. He was a recipient of the Dean's Doctoral Student Assistantship, a Gotshall Fellowship, and a P. C. Rossin Doctoral Fellow at Lehigh University.



interests include optical wireless communications, multiple input and multiple output technology, interference alignment, and wireless indoor localization.

**Liang Wu** (Senior Member, IEEE) received the B.S., M.S., and Ph.D. degrees from the School of Information Science and Engineering, Southeast University, Nanjing, China, in 2007, 2010, and 2013, respectively. From September 2011 to March 2013, he was with the School of Electrical Engineering and Computer Science, Oregon State University, as a Visiting Ph.D. Student. In September 2013, he joined the National Mobile Communications Research Laboratory, Southeast University, where he has been an Associate Professor, since April 2018. His research



currently an Associate Professor. His research interests include signal processing in wireless communications and optical mobile communications.

**Jian Dang** (Senior Member, IEEE) received the B.S. degree in information engineering and the Ph.D. degree in information and communications engineering from Southeast University, Nanjing, China, in July 2007 and September 2013, respectively. From September 2010 to March 2012, he was with the Department of Electrical and Computer Engineering, University of Florida, Gainesville, FL, USA, as a Visiting Scholar. Since September 2013, he has been with the National Mobile Communications Research Laboratory, Southeast University, where he is